

**EFFECTS OF INDUCED ACOUSTIC VIBRATIONS ON DROPLET SHEDDING
ON HYBRID MICRO-STRUCTURED SURFACES**

A Thesis

by

CHEN-LING LAI

Submitted to the Office of Graduate and Professional Studies of
Texas A&M University
in partial fulfillment of the requirements for the degree of

MASTER OF SCIENCE

Chair of Committee,	Jorge L. Alvarado
Committee Members,	Michael Pate
	Hae-Kwon Jeong
Head of Department,	Andreas A. Polycarpou

May 2014

Major Subject: Mechanical Engineering

Copyright 2014 Chen-Ling Lai

ABSTRACT

Artificial hydrophobic and superhydrophobic surfaces have been studied in the last ten years in an effort to understand the effects of structured micro- and nano-scale features on droplet motion and self-cleaning mechanisms. Among these structured surfaces, hybrid surfaces consisting of a combination of hydrophilic and hydrophobic materials have been designed, fabricated and characterized to understand how surface properties and morphology affect enhanced droplet growth rates and droplet shedding during condensation. However, use of hybrid surfaces in condensation leads to a strong pinning effect that takes place between the condensing droplets and the hydrophobic-hydrophilic edge, leading to a significant contact angle hysteresis effect. In an effort to circumvent the pinning effect, a vibration-induced droplet shedding method has been explored to overcome contact angle hysteresis and facilitate droplet shedding at lower rolling angles.

To understand the effects of hybrid surface morphology and vibration modes on droplet removal from surfaces used for condensation, this research study focuses on the effects of acoustic-induced vibrations on droplet sliding at different inclined angles on hybrid surfaces. A hydrophilic surface (silicon surface) has been used as the baseline in the study to be able to uncover the effects of vibration on pinned droplets. Firstly, the relationship between sliding angles and droplet volume was investigated experimentally for hybrid surfaces with different spacings. Then, the effects of natural resonance frequencies of droplets with different volumes on

different surfaces were also studied using a resonance model and a customized experimental setup. Acoustic-induced vibrations were then applied to the surfaces to understand the effects of single or multiple resonance frequencies on droplet sliding angles. Droplet vibration and roll-off processes were experimentally characterized using a high speed imaging system. An acoustic sensor was also used to measure the induced frequencies and amplitudes.

Experimental results to date show that hybrid surfaces with larger spacing leads to lower droplet sliding angles. Furthermore, droplets under the influence of acoustic waves depict different contour morphologies when vibrating at different resonance frequencies. Moreover, droplet sliding angles can be reduced through vibration when the proper combination of droplet size and surface morphology is prescribed. Future studies will consider the use of acoustic waves in actual condensers.

DEDICATION

To Dr. Jorge L. Alvarado for his inspiration and support

To my family for their unconditional love

ACKNOWLEDGEMENTS

I would like to thank my committee chair, Dr. Jorge L. Alvarado, and my committee members, Dr. Michael Pate, Dr. Hae-Kwon Jeong, for their guidance and support throughout the course of this research.

Thanks also go to my friends and colleagues and the department faculty and staff for making my time at Texas A&M University a great experience. I also appreciate Chun-Wei Yao, Ph.D. student, for his guidance throughout this research.

Finally, thanks to my mother for her encouragement, patience and love.

NOMENCLATURE

A	Area
g	Gravitational acceleration
j	Resonance mode
m	weight of the droplet
p	Half arc length of a droplet
q_j	Wave factor for one dimensional capillary-gravity wave
R	Droplet radius
r_f	roughness factor
V	Droplet volume
γ	Surface tension
θ_0	Intrinsic contact angel
θ_A	Advancing angle
θ_{CB}	Apparent contact angle on a heterogeneous surface
θ_R	Receding angle
θ_W	Apparent contact angle on a rough surface
ρ	Density of droplet
φ_1	Ratio of the liquid-vapor interfacial area to the projected area
φ_2	Ratio of the liquid-solid interfacial area to the projected area
ω	Resonance frequency

Subscript:

j	Resonance mode
L	Liquid
S	Solid
V	Vapor

TABLE OF CONTENTS

	Page
ABSTRACT	ii
DEDICATION	iv
ACKNOWLEDGEMENTS	v
NOMENCLATURE	vi
TABLE OF CONTENTS	viii
LIST OF FIGURES	x
LIST OF TABLES	xiii
1. INTRODUCTION	1
1.1 Motivation	1
1.2 Objectives	2
2. BACKGROUND AND LITERATURE REVIEW	3
2.1 Fundamental theories of liquid micro-droplets	3
2.1.1 Contact angles and wettability	3
2.1.2 Surface tension and surface free energy	7
2.1.3 Hysteresis effect	7
2.2 Sliding behavior of droplets on an inclined surface	8
2.3 Vibrations of free liquid droplets	12
2.3.1 Prediction of droplet resonance frequencies	12
2.3.2 Wetting transition and droplet motion induced by mechanical vibration	16
2.4 Conclusion	18
3. EXPERIMENT SETUP AND PROCEDURE	19
3.1 Tilting stage system	20
3.2 Acoustic vibration system	22
3.3 Data acquisition system (DAQ system)	23
3.4 Image capture system	25

3.5 Hybrid surface	26
3.6 Procedures	28
3.6.1 Contact angle measurement	28
3.6.2 Sliding angle measurement	29
3.6.3 Resonance frequency of impinged droplets	29
3.6.3.1 Theoretical values of droplet resonance frequency	29
3.6.3.2 Experimental values of droplet resonance frequency	31
3.6.3 Sliding angle measurement with resonance-based vibration	31
4. RESULTS AND DISCUSSION	33
4.1 Wetting characteristics of droplets on hybrid surfaces	33
4.1.1 Measured contact angles	33
4.1.2 Measured sliding angles	37
4.2 Resonance frequency of droplets	39
4.2.1 Calculated resonance frequency values and expected vibration behavior	39
4.2.2 Experimental resonance frequency values and droplet resonance behavior ...	41
4.2.3 Natural resonance frequency mode adjustments for optimal droplet vibration	43
4.3 Sliding angles under various vibrated conditions	50
4.3.1 Effects of mono-resonance frequency	50
4.3.2 Effects of 1 st resonance amplitude	55
4.3.3 Effects of multi-resonance frequencies	58
5. CONCLUSION	62
REFERENCES	65

LIST OF FIGURES

	Page
Fig. 2-1 Schematic drawing of side view of (a) a droplet on the hydrophobic surface (b) a droplet on the hydrophilic surface	4
Fig. 2-2 Schematic drawing of droplet contact modes (a) on the ideal surface (b) for homogeneous wetting (c) for heterogeneous wetting	5
Fig. 2-3 Schematic drawing of the receding angle and the advancing angle of a droplet	8
Fig. 2-4 Schematic illustration of the surface model with a series of uniform needles used in Miwa et al. (2000) [19].....	10
Fig. 2-5 Schematic drawing of the half arc length (p) of a droplet [31]	14
Fig. 2-6 Schematic drawing of a droplet for the model Boreyko et al. developed [13]...	14
Fig. 2-7 Numerical values obtained for $h(\theta)$ [32]	15
Fig. 3-1 Experimental Apparatus I.....	19
Fig. 3-2 Experimental Apparatus II.....	20
Fig. 3-3 Schematic illustration of the tilting stage system	21
Fig. 3-4 Image of the tilting stage system	21
Fig. 3-5 Schematic drawing of some system-operation examples	22
Fig. 3-6 Image of the speaker (Infinity Reference 860w, Infinity Inc.).....	23
Fig. 3-7 Image of data reading with LabVIEW programming.....	24
Fig. 3-8 Calibration curve of the output frequency and the input frequency	25
Fig. 3-9 Image of the high speed camera used in this research.....	26
Fig. 3-10 Schematic drawings of (a) side view of the hybrid surface, (b) top view of a hybrid surface, where a_1 is the width of hydrophilic material, a_2 is the width of hydrophobic material [33]	27

Fig. 3-11 SEM images of a hybrid surfaces with a micropillar array with spacing values of (a) 25 μm (b) 37.5 μm , and (c) 50 μm [33]	27
Fig. 3-12 Image of the contact angle measurement for 5- μm droplet on the hybrid surface with 25- μm spacing value.....	28
Fig. 3-13 Schematic drawing of a droplet with parameters used in the theoretical model [13]	30
Fig. 4-1. Apparent contact angle measurement of three droplet volumes on a hybrid surface with 50 μm spacing.....	34
Fig. 4-2 Apparent contact angles of droplets with different volumes on different hybrid surfaces	35
Fig. 4-3 Original sliding angles of droplets with different droplet volumes on different surfaces. Note: zero spacing represents the baseline (i.e. silicon wafer)	38
Fig. 4-4 Schematic drawing of expected droplet motions (a) without vibration (at static equilibrium), (b) at the first resonance frequency ($j = 1.5$), (c) at the second resonance frequency ($j = 2.0$). The dash line in (b) and (c) represents the droplet contour at static equilibrium.	40
Fig. 4-5 Droplet resonance motions on the 25 μm -spacing hybrid surface	42
Fig. 4-6 Schematic drawing of expected droplet motions (a) at the first resonance frequency ($j = 1.5$, 3 nodes), (b) at the second resonance frequency ($j = 2.0$, 4 nodes). The dash line in (a) and (b) represents the droplet contour at static equilibrium, and the black spots emphasizes the nodes.	45
Fig. 4-7 Experimental image and schematic drawing of the first resonance frequency for each droplet volume on a 25 μm -spacing hybrid surface.....	46
Fig. 4-8 Experimental image and schematic drawing of the second resonance frequency for each droplet volume on a 25 μm -spacing hybrid surface.....	47
Fig. 4-9 The configuration of (a) 5 μL , (b) 10 μL , (c) 15 μL droplet on the hybrid surface with 50- μm spacing	49
Fig. 4-10 Sliding angle of 5 μL droplet vibrating at different resonance frequencies	52
Fig. 4-11 Sliding angle of 10 μL droplet vibrating at different resonance frequencies ...	52
Fig. 4-12 Sliding angle of 15 μL droplet vibrating at different resonance frequencies ...	53

Fig. 4-13 Sliding angle of 5 μL droplet vibrating at the first resonance frequencies with different amplitudes	56
Fig. 4-14 Sliding angle of 10 μL droplet vibrating at the first resonance frequencies with different amplitudes	57
Fig. 4-15 Sliding angle of 15 μL droplet vibrating at the first resonance frequencies with different amplitudes	57
Fig. 4-16 Sliding angle of 5 μL droplet vibrating at mono- or multi- resonance frequencies	60

LIST OF TABLES

	Page
Table 4-1 Apparent contact angles of droplets with different volumes on different surfaces	34
Table 4-2 Original sliding angles of droplets with different volumes on different surfaces.....	37
Table 4-3 Calculated frequency values for droplet resonance for different droplet volumes on different surfaces	39
Table 4-4 Experimental frequency values for droplet resonance for different droplet volumes on different surfaces	41
Table 4-5 Calculated and experimental first resonance frequencies for 10 μL and 15 μL droplets	44
Table 4-6 Droplet sliding angles measured at different mono- resonance frequencies. Note: “DS” means that droplets stick on the surface, and “N/A” means that the experiment was not undertaken due to the limitation of instruments.	51
Table 4-7 Droplet sliding angles measured at the first resonance frequency with different amplitudes	55
Table 4-8 Sliding angles of 5 μL droplets measured at mono- or multi- resonance frequencies	58
Table 4-9 Sliding angles of droplets with three different volumes measured at mono- or multi-resonance frequencies on a hybrid surface with 25 μm spacing.....	60

1. INTRODUCTION

1.1 Motivation

Artificial hydrophobic and superhydrophobic surfaces have been studied in the last ten years in an effort to understand the effects of micro- and nano-scale structures on droplet motion and self-cleaning mechanisms. Such surfaces are characterized by having high contact angles and low contact angle hysteresis, resulting in easy liquid-shedding, preferably during condensation [1, 2]. Recent studies [3, 4] have revealed that enhanced dropwise condensation occurs once nucleation has taken place. However, hydrophobic surfaces exhibit lower nucleation rates because of higher contact angles and a higher nucleation energy barrier [5]. Hybrid surfaces, consisting of a combination of hydrophilic and hydrophobic materials, were designed, fabricated and characterized to enhance droplet nucleation, droplet growth rates and droplet shedding during condensation [6-10].

Droplet shedding on hybrid surfaces, however, is limited because the pinning effect that occurs between the condensing droplets and the hydrophobic-hydrophilic edge, leading to a significant contact angle hysteresis effect. An external force is thereby required to minimize or eliminate the hysteresis effect. Previous studies [11-16] show that using acoustic vibration is an effective way to induce droplet shedding by forcing wetting transition from the Wenzel to the Cassie-Baxter state. Once the energy barrier associated with the pinning effect has been overcome through induced vibration, droplets are able to shed from the surfaces. Therefore, acoustic induced vibration of

droplets has been found to be a feasible method to resolve the problem of the pinning effect on hybrid surfaces.

Even though the vibration-induced wetting transition was investigated in some recent studies, the vibration mechanism of droplet shedding has not yet been fully understood. This research quantitatively considers the effect of acoustic vibration on droplet sliding angles under various vibration resonance conditions, providing a possible way to effectively shed droplet off hydrophobic-hydrophilic hybrid surfaces with high contact angle hysteresis.

1.2 Objectives

The specific objectives of this research were to understand the effects of hybrid surface morphology and acoustic vibration on droplet removal from surfaces used for condensation. This study focused on the effects of acoustic-induced vibrations on droplet sliding at different inclined angles on hybrid surfaces. The relationship between droplet sliding angles and droplet volumes was firstly investigated through experimentation. Then, the effects of natural resonance frequencies of droplets with different volumes on different surfaces were also studied and analyzed using a resonance model and a customized experimental setup. Acoustic-induced vibrations were then applied to the surfaces to understand the effects of single or multiple resonance frequencies on droplet sliding angles. Droplet vibration and sliding processes were experimentally characterized using a high speed imaging system and an acoustic sensing device.

2. BACKGROUND AND LITERATURE REVIEW

2.1 Fundamental theories of liquid micro-droplets

The wetting characteristics of droplets have been described and analyzed using the Cassie and Wenzel theories. Droplets on the Cassie state, the state in which there are air pockets between the droplets and the bottom of a micro-structure, are much easier to leave surfaces than when they are on the Wenzel state, the state in which the droplet will wet the entire liquid-solid interfacial structure. The transition between wetting regimes (i.e. transition from the Wenzel to the Cassie state) is one of the main causes that affects contact angle hysteresis of droplets on the surfaces, which affects droplet mobility. This section introduces the fundamental theories related to droplet wettability and contact angle hysteresis, which are helpful in the understanding of the mechanisms that lead to droplet's contact angle hysteresis.

2.1.1 Contact angles and wettability

From the established wettability theories, one is able to calculate the droplet contact angles when droplets sit on wettable and non-wettable surfaces. Contact angles of droplets are related to surface tension by using the Young's equation, which relates surface tension forces between the different phases and the intrinsic contact angle (θ_0) when a droplet is at static equilibrium [17]. The Young's equation is as follows:

$$\cos\theta_0 = \frac{\gamma_{SV} - \gamma_{SL}}{\gamma_{LV}} \quad (2-1)$$

Where γ_{SV} , γ_{SL} , and γ_{LV} are the surface tension between the solid and vapor phases, solid and liquid phases, and liquid and vapor phases, respectively. As shown in Fig. 2-1, if θ_0 is greater than 90° , the surface is considered to be hydrophobic; contrarily, it is hydrophilic.

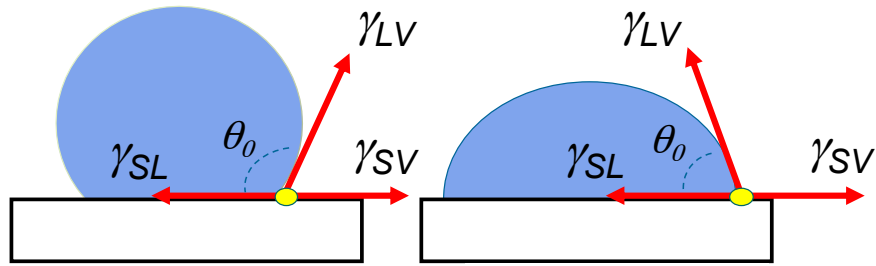


Fig. 2-1 Schematic drawing of side view of (a) a droplet on the hydrophobic surface (b) a droplet on the hydrophilic surface

The Young's equation for any ideal surface, however, it is not enough to accurately describe the wetting characteristics of droplet on most surfaces in nature. Since there are various micro- or nano-structures existing on real surfaces, such as papillae, fold, and pores, which exhibits different surface roughness, Wenzel (1936) [18] and Cassie-Baxter (1944) [10] revised the Young's equation to take into account homogeneous and heterogeneous wetting behavior on non-ideal surfaces.

Wenzel proposed a model to describe homogeneous wetting regime as shown in Fig. 2-2(b) [18]. The Wenzel model is as follows:

$$\cos\theta_w = r_f \cos\theta_0 \quad (2-2)$$

$$r_f = \frac{A_{act}}{A_{pro}} \quad (2-3)$$

Where θ_w is the apparent contact angle on a rough surface, θ_0 is the intrinsic contact angle acquired from the Young's equation, and the roughness factor, r_f , is defined as the ratio of actual contact area between the droplet and the solid surface to the projected area. By definition, roughness factor r_f is either equal or greater than 1, which means surface roughness will strengthen either the hydrophobicity or hydrophilicity of the surface with respect to the droplet.

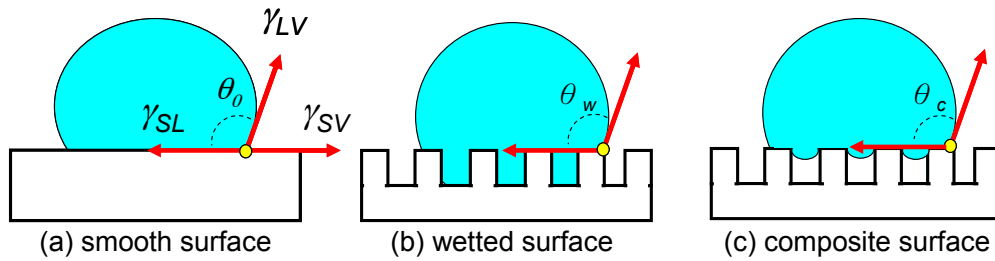


Fig. 2-2 Schematic drawing of droplet contact modes (a) on the ideal surface (b) for homogeneous wetting (c) for heterogeneous wetting

However, the Wenzel model is not sufficient enough to account for the heterogeneous nature of rough surfaces. As seen in Fig. 2-2(c), air is trapped between the droplet and the surface structure, resulting in the composite surface formed by the liquid-solid and vapor-solid interfaces. The Cassie-Baxter equation was developed to explain heterogeneous wetting as shown below [10].

$$\cos\theta_{CB} = \varphi_1 \cos\theta_0 + \varphi_2 \cos\theta_1 \quad (2-4)$$

$$\varphi_1 + \varphi_2 = 1 \quad (2-5)$$

$$\varphi_1 = \frac{A_{S-L}}{A_{pro}} \quad (2-6)$$

$$\varphi_2 = \frac{A_{G-L}}{A_{pro}} \quad (2-7)$$

Where θ_{CB} is the apparent contact angle on a heterogeneous surface, θ_0 is the intrinsic contact angle of the liquid-solid interface, and θ_1 is the intrinsic contact angle of the liquid-vapor interface. The φ_1 is the ratio of the liquid-vapor interfacial area to the projected area, and the φ_2 is the ratio of the liquid-solid interfacial area to the projected area. Drop shape is assumed to be spherical in air, thus θ_1 is thereby 180° . Based on this assumption, Miwa et al. (2000) simplified the Cassie-Baxter equation (2-4) with the following [19]:

$$\cos\theta_{CB} = \varphi_1 \cos\theta_0 + \varphi_1 - 1 \quad (2-8)$$

By taking into account the roughness ratio (r), the Cassie-Baxter equation can be modified as follows:

$$\cos\theta_{CB} = r\varphi_1 \cos\theta_0 + \varphi_1 - 1 \quad (2-9)$$

If $r = r_f$ and $\varphi_1 = 1$, then Cassie-Baxter equation changes to the Wenzel equation.

2.1.2 Surface tension and surface free energy

Surface free energy is the product of surface tension and contact area as a droplet wets a surface. Because of the significant difference in density between liquid and gas phases, liquid molecules at the liquid-surface interface are pulled inwards and therefore create tension which is called “surface tension.” In terms of energy, a minimum amount of surface energy is required to create one unit of surface area, which is called “surface energy.”

A droplet is favorable to exist with intrinsically lower surface energy without any external energy. Patankar (2003) proposed a theorem of surface free energy to determine droplet contact modes based on the lowest energy level; however, a droplet does not always exist in the lower energy state. More accurately, the state where a droplet will remain lies on how the droplet is formed [20]. Patankar (2004) also investigated drop transition from the Cassie state to the Wenzel state, and proposed a methodology to determine the required energy barrier for the transition of state [21].

2.1.3 Hysteresis effect

Hysteresis is the energy barrier that prevents dynamic behaviors or transitions of droplets on surfaces. If the surface containing a droplet at rest is slowly inclined, the droplet will begin to move at a specific angle of inclination, which defined as a “sliding angle.” At the moment that the droplet begins to move, the contour curvatures of the droplet on the left and right sides are different, as shown in Fig. 2-3. The right contact angle is the called the advancing angle (θ_A), while the left one is the receding angle (θ_R).

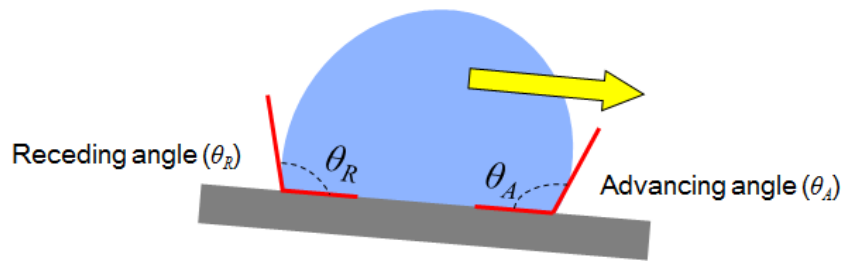


Fig. 2-3 Schematic drawing of the receding angle and the advancing angle of a droplet

Albenge et al. (2002) described the “hysteresis effect,” as the process by which a droplet contour changes from its static equilibrium shape to one characterized by advancing and receding angles. Furthermore, droplet contact angle hysteresis is defined as the difference between the advancing and receding angles [22].

$$\Delta\theta = \theta_A - \theta_R \quad (2-10)$$

From the energy point of view, droplets should overcome the energy barrier caused by the hysteresis effect in order to move or roll off a surface.

2.2 Sliding behavior of droplets on an inclined surface

The sliding behavior of droplets sitting on inclined surfaces has been studied in detail for many years. It is well understood that droplets have to overcome the energy barrier associated with the hysteresis effect before they can move or roll off a surface. The effect of roughness on droplet wetting behavior has been studied and analyzed using the modified Cassie-Baxter and Wenzel equations as explained above. However, effect of roughness on droplet mobility has recently renewed received attention in the heat

transfer community. Miwa et al. (2000) investigated the effects of the surface roughness on sliding angles of water droplets on superhydrophobic surfaces. At higher levels of hydrophobicity, the droplet sliding angle decreases while the contact angle increases [19]. Miwa et al. derived an equation (2-11) to describe the relationship between sliding angles and contact angles on superhydrophobic surface by taking into account surface roughness.

$$\sin \alpha = \frac{2rk \sin \theta' (\cos \theta' + 1)}{g(r \cos \theta + 1)} \left\{ \frac{3\pi^2}{m^2 \rho (2 - 3 \cos \theta' + \cos^3 \theta')} \right\}^{1/3} \quad (2-11)$$

Here α is the sliding angle, θ' is the equilibrium contact angle on a rough surface, and θ is the equilibrium contact angle on a flat surface. The ρ is density of water, m is the weight of the droplet, and g is the gravitational acceleration. The r presents the ratio of the side area to the bottom area of the needle represented by a/b as shown in Fig. 2-4, and k is proportionality constant as shown in the following equation.

$$k = \left\{ \frac{9m^2(2 - 3 \cos \theta + \cos^3 \theta)}{\pi^2} \right\}^{1/3} \frac{\sin \alpha (g\rho^{1/3})}{6 \sin \theta} \quad (2-12)$$

The constant value k can be obtained by measuring α , θ , and m values for any flat surface. The calculated sliding angles when using Equation 2-11 agree well with the experimental results [19].

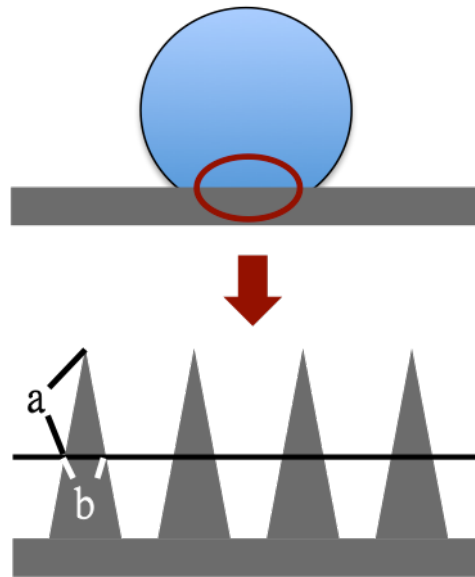


Fig. 2-4 Schematic illustration of the surface model with a series of uniform needles used in Miwa et al. (2000) [19]

Hyväluoma et al. (2007) simulated the behavior of droplets on inclined heterogeneous surfaces by the lattice- Boltzmann method using the Shan-Chen multiphase model. The simulation results showed that increased roughness leads to larger contact angle hysteresis, and increased hydrophobicity of these surfaces decreases contact angle hysteresis. This study also considered droplet sliding on an anisotropic surface and concluded that contact angle hysteresis may vary significantly depending on the direction in which the surface is tilted regardless of initial droplet shape and identical apparent contact angles [23].

Öner and McCarthy (2000) proposed that the proper design of the three-phase (solid-water-air) contact line is a crucial factor to lower the energy barrier for droplet motions and thereby improve the sliding behaviors of droplets [24]. Yoshimitsu et al. (2002) found out that the length and continuity of the three-phase contact line on a

surface also influence the sliding behavior of water droplets. It was also observed that a continuous short three-phase contact line is ideal for excellent droplet-shedding behavior [25]. Yoshimitsu et al. compared the sliding behavior of water droplets on surfaces with pillar-like and groove structures. They found out that the surface with groove structures leads to better droplet-shedding in the parallel direction of the grooves, because the three-phase line toward the sliding direction is continuous. The three-phase line that droplets make when sitting on a surface containing pillar-like structures is discontinuous which results in greater sliding angles [25].

ElSherbini and Jacobi (2004) found that contact angle variation along the periphery of the droplet contour was best fitted by a third-degree polynomial function after testing droplets on eight surfaces. Based on this finding, ElSherbini and Jacobi (2004) developed a general relation between advancing contact angle, receding contact angle, and the maximum Bond number for a liquid–surface combination on inclined plane surfaces [26].

Annapragada et al. (2012) developed a pseudo-Lagrangian methodology based on the Volume Of Fluid - Continuous Surface Force (VOF-CSF) model to simulate droplet motion down on an inclined surface. The terminal velocity of droplets is predicted through this model and agrees with the experimental results [27]

2.3 Vibrations of free liquid droplets

Vibrations have been considered as an effective way to induce droplet motions on surfaces. The following sections review previous studies to understand the effects of droplet resonance frequencies and how vibration affects wetting transition of droplets in motion.

2.3.1 Prediction of droplet resonance frequencies

The vibrations of spherical liquid droplets have been studied more than a century ago by Kelvin [28] and Rayleigh [29]. Lamb (1932) established a general expression for different resonance modes of oscillated spherical-droplets as follows [30]:

$$f_n = \sqrt{\frac{n(n-1)(n+2)}{3\pi\rho V}} \quad (2-13)$$

Where f_n is the frequency for the resonance mode n , ρ is the density of the liquid, γ is the surface tension, and V is the droplet volume. However, the Lamb equation is not sufficient to describe the case of sessile droplets partially contacting or wetting a substrate. In other words, the droplet shape was not taken into account in the development of the Lamb model. Very few studies have considered the effect of droplet oscillation on droplet contact line.

Noblin et al. (2004) proposed a model that considers both droplet contact angle and the contact line. In their study, two regimes of axisymmetric drop oscillations were observed including Type-I, where the contact line remained fixed at low amplitude, and

Type-II, where the contact lined oscillated and appeared above the threshold amplitude [31]. For Type-I modes, the resonance frequency ω_j with immobile contact line can be predicted as follows [31]:

$$\omega_j^2 = \left(g q_j + \frac{\gamma}{\rho} q_j^3 \right) \tanh \left(q_j \frac{V}{\pi a^2} \right) \quad (2-14)$$

Where j is resonance mode number, g is the gravitational acceleration, γ is the surface tension, ρ is the density of the droplet, V is the drop volume, and a is the drop contact radius. The wave factor q_j for one dimensional capillary-gravity wave is as follows:

$$q_j = \frac{\pi(j-0.5)}{p} \quad (2-15)$$

Here p is the half arc length of a droplet, depending on the drop volume and contact angle as shown in Fig. 2-5. Since there was no analytical expression for p values in general, Noblin et al. (year) performed numerical calculation for various droplet profiles to acquire the values of p .

For Type-II modes, the contact angle variations induced by vibration can overcome the contact angle hysteresis which makes the drop contact line mobile. This study assumed a perfectly smooth surface, where there was no hysteresis and no viscous dissipation, and the wave factor q_k corresponding to resonance mode number k is as follows [31]:

$$q_j = \frac{k\pi}{p} \quad (2-16)$$

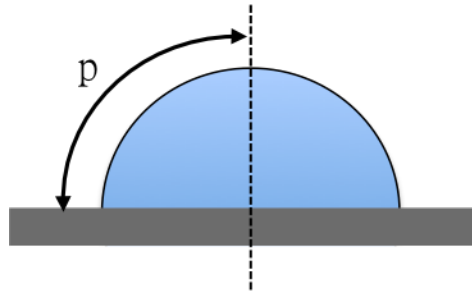


Fig. 2-5 Schematic drawing of the half arc length (p) of a droplet [31]

Boreyko et al. (2009) derived an analytical expression for p in Type-I cases as follows [13]:

$$p = R\theta \quad (2-17)$$

Where R is the droplet radius related to the droplet volume (V) and the apparent contact angle (θ) as shown in Fig. 2-6.

$$R = \left(\frac{3V}{\pi(1 - \cos \theta)^2(2 + \cos \theta)} \right) \quad (2-18)$$

In their study, the calculated values agreed with the experimental results.

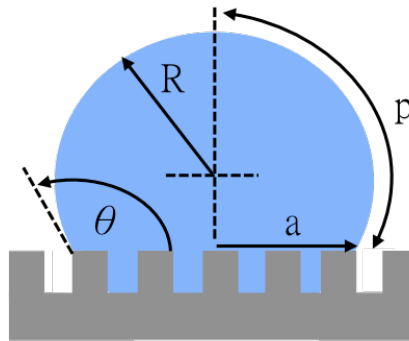


Fig. 2-6 Schematic drawing of a droplet for the model Boreyko et al. developed [13]

Celestini and Kofman (2006) used a simple oscillator model to derive a semianalytical expression for the eigenfrequency ω_0 of a supported droplet, and a scaling law of the energy dissipation as follows [32]:

$$\omega_0 = \sqrt{\frac{6\gamma h(\theta)}{\rho(1-\cos\theta)(2+\cos\theta)}} R^{-3/2} \quad (2-19)$$

Where θ is droplet wetting angle, and $h(\theta)$ was computed by the authors as shown in Fig. 2-7.

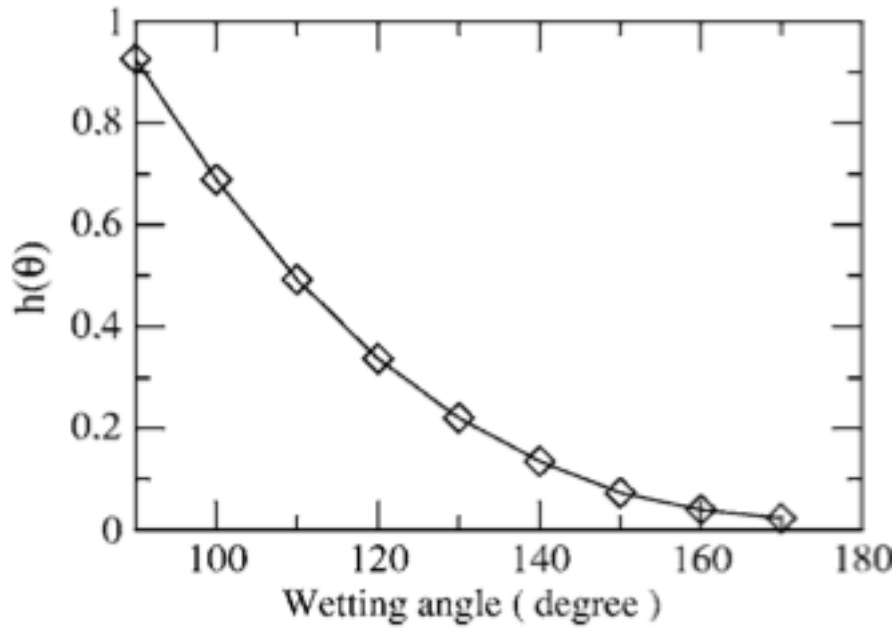


Fig. 2-7 Numerical values obtained for $h(\theta)$ [32]

The experimental results obtained for mercury drop on glass surface agreed with the predicted values of resonance frequencies the drop when radius was greater 0.1 mm [32].

Ramos (2008) also used this semiempirical model to bring into agreement the measured and calculated frequency values for water droplets on amorphous-silica (a-SiO₂) nano-structured surface [16].

2.3.2 Wetting transition and droplet motion induced by mechanical vibration

The contact behavior of droplets on roughness surfaces can be changed with vibration. Bormashenko et al. (2007, 2007) observed Cassie-Wenzel transition when a liquid droplet was placed on a polymer honeycomb pattern under the action of vibration [11, 14]. Furthermore, the authors predicted the resonance frequencies via the simple model developed by Noblin et al. [31], and the calculated values coincide with the experimentally established resonance frequencies. This research also concluded that the resonance wetting transition is related to the behavior of the triple line caused by both the inertia force and the increase in the Laplace pressure [11, 14].

Ramos (2008) reported the effects on both a-SiO₂-layers surfaces with a controlled hydrophobicity and the vibration modes of submillimeter drops supported by such surfaces. These two parameters resulted in a drastic reduction in the contact angle hysteresis and substantially increased the mobility of the supported droplets [16].

Boreyko et al. (2009) took advantage of mechanical vibration to induce Wenzel to Cassie wetting transition. They performed experiments on a lotus leaf which was sticky to the water drops after condensation on a cold plate. The experimental results showed that the kinetic energy caused by vibration was converted to surface energy which was used to overcome the adhesive work of droplets. It is plausible that antide

superhydrophobicity of lotus leaves can be reached through this vibration-induced wetting transition [13].

Jung and Bhushan (2009) investigated the Cassie to Wenzel wetting transition induced by drop dynamic effects, such as bouncing and vibration, which may disrupt the composite solid-air-liquid interface. In the bouncing study, it was observed that the transition easily happened due to a larger-distance dynamic impact on the surface. In the vibration study, the inertia force of the vibrated droplets could overcome the adhesion force and the droplets could bounce off the surface before the Cassie to Wenzel wetting transition occurred. Moreover, this study also showed that the hierarchical-structured surface had a much better ability to counteract the dynamic effects and the composite solid-air-liquid interface was able to remain stable [15].

Brunet et al. (2007) reported on an experimental study of glycerol-water mixture drop vibrated vertically on an inclined plexiglass substrate (without surface treatment). Droplets with different kinematic viscosities (31-55 mm²/s) were tested. The resulting drop motions depended on the values of amplitudes and frequencies used. In summary the droplets could move down the substrate (sliding), remained stationary (static) or moved up the substrate (climbing) depending on the imposed conditions. From the study, phase diagrams for different drop volumes, viscosities, and angles of the inclined surface were obtained. In their experiments, droplet experienced an upward motion above when threshold in vibration acceleration was exceeded. For the drops with lower viscosities (such as water drops, 1.004 mm²/s), the drops broke up before the onset of climbing [12].

2.4 Conclusion

Previous studies mainly focused on the effects of surface roughness and the motion of the three-phase contact line on droplet mobility. For structured surfaces, however, the effects of acoustic vibration on water droplet sliding behaviors have not yet been fully investigated. Thus, this study investigates the relationship between droplet sliding angles and vibration modes, providing a possible way to effectively shed droplets on hydrophobic-hydrophilic hybrid surfaces with high contact angle hysteresis.

3. EXPERIMENT SETUP AND PROCEDURE

In order to achieve the objectives of this research project, an experimental setup has been designed and built for the sliding-angle experiment with or without the use of acoustic vibration. The experimental setup consists of four main systems: tilting stage system, acoustic vibration system, data acquisition system, and image capture system as shown in Fig. 3-1 and Fig. 3-2.

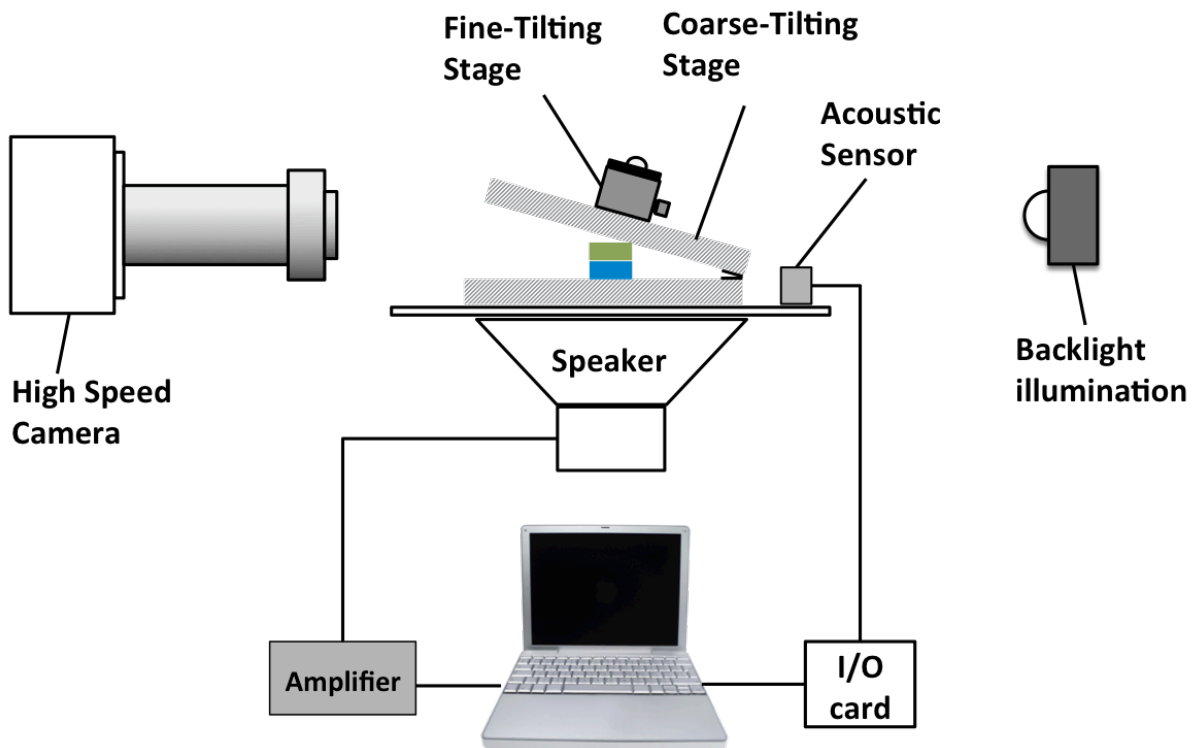


Fig. 3-1 Experimental Apparatus I

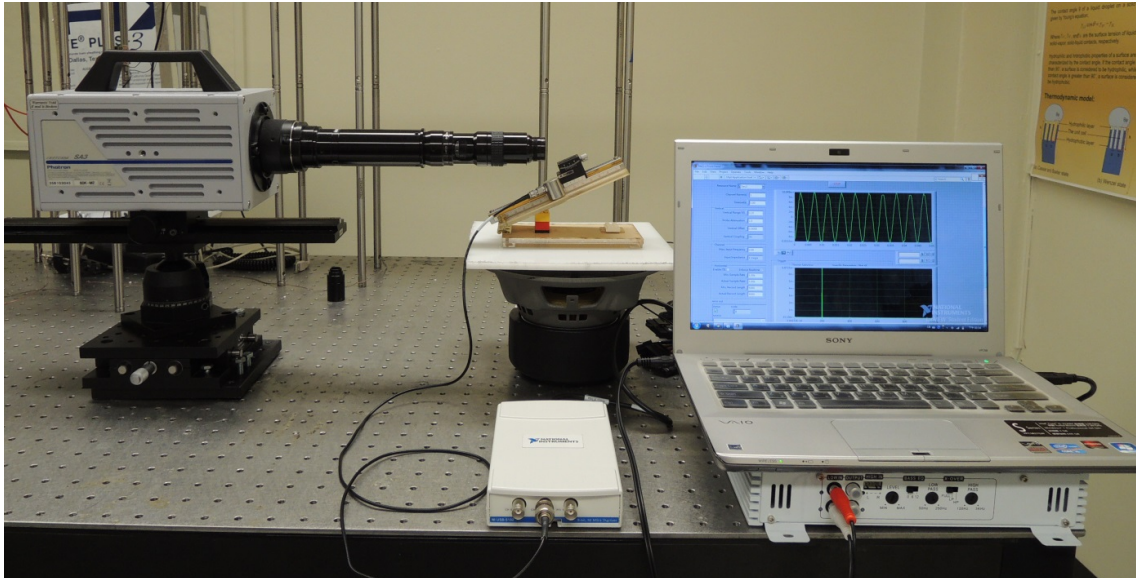


Fig. 3-2 Experimental Apparatus II

3.1 Tilting stage system

In this study, a customized stage, including coarse-tilting and fine-tilting stages, were made with controllable inclined angles as shown in Fig. 3-3 and Fig. 3-4. The inclined angle of this tilting stage can be tuned by using either the coarse or fine adjustment.

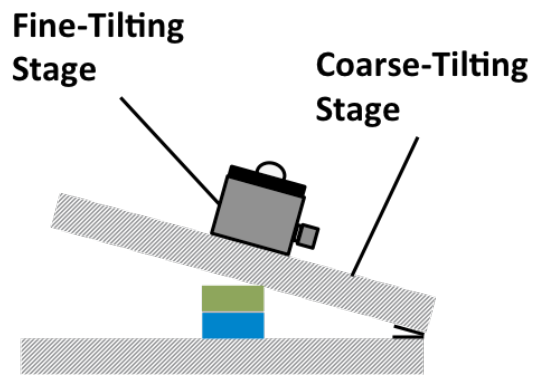


Fig. 3-3 Schematic illustration of the tilting stage system

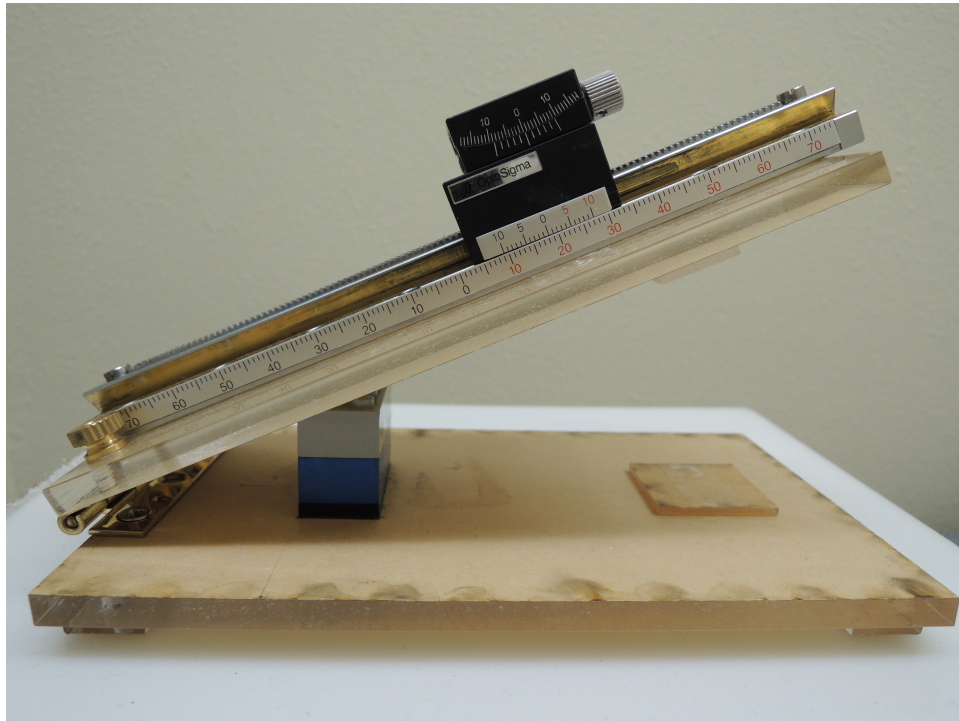


Fig. 3-4 Image of the tilting stage system

The coarse-tilting stage was homemade, where plastic blocks (Lego's) were used to provide discrete inclined angles at 10° , 30° , 50° , 70° . Above the coarse-tilting stage, a goniometer (OptoSigma Inc.) was used as the fine-tilting stage, which had a tilting angle

range of $\pm 15^\circ$. The fine-tilting stage could continuously change inclined angles from -15° to $+15^\circ$ in addition to the angle provided by the coarse stage. The composite tilting stage system was completely adjustable in the range of 0° to 90° . Some examples of the cases considered are as shown in Fig. 3-5.

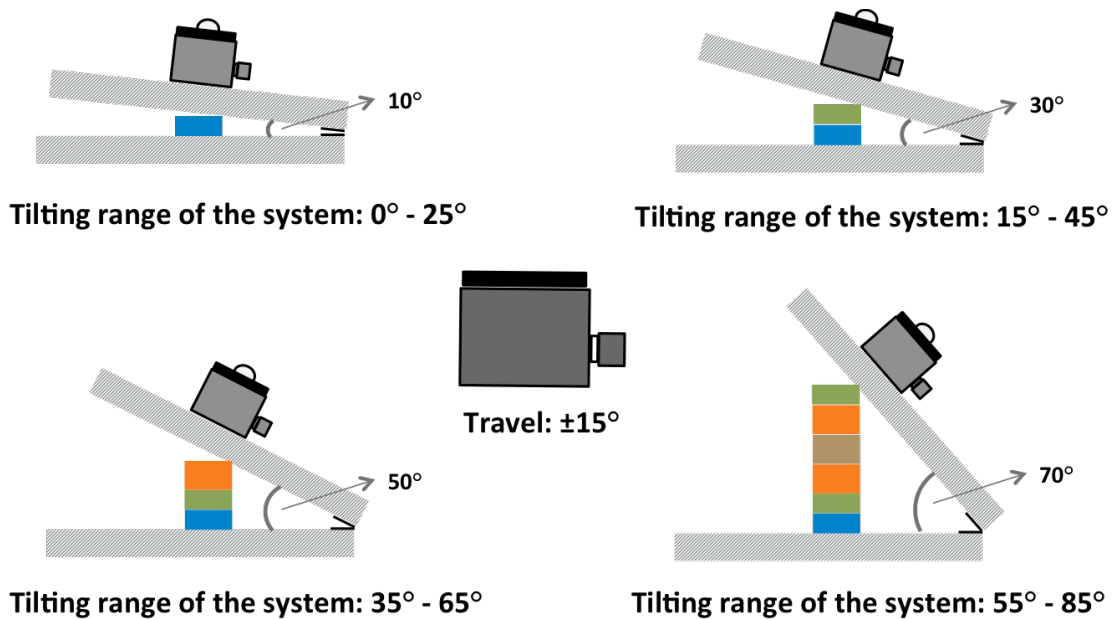


Fig. 3-5 Schematic drawing of some system-operation examples

3.2 Acoustic vibration system

An 8-in subwoofer with 1000-watts peak power handling (Infinity Reference 860w, Infinity Inc.) was utilized to provide vertical vibrations as shown in Fig. 3-6. The frequency response of the speaker was varied from 30 Hz to 400 Hz. A computer was used to control the speaker and display specific frequencies with the tone generator software (Tone Generator Software, NCH Inc.)



Fig. 3-6 Image of the speaker (Infinity Reference 860w, Infinity Inc.)

3.3 Data acquisition system (DAQ system)

An accelerometer (Model 1000A, MISTRAS group Inc.) with a power supply (P5000, MISTRAS group Inc.) was used as the acoustic sensor to detect the vibration signals of the vibrated substrate during the vibration experiments. The sensor was attached on the tilting stage to measure the frequencies and amplitudes of the induced acoustic vibrations.

An NI-card (NI USB-5132, NATIONAL INSTRUMENTS Inc.) was used to fetch the data detected by the sensor, which was connected between the sensor and the computer. The acquired signals were then digitally analyzed using LabVIEW, which was used to obtain the numerical values of the vibration frequencies and amplitude as shown in Fig. 3-7.

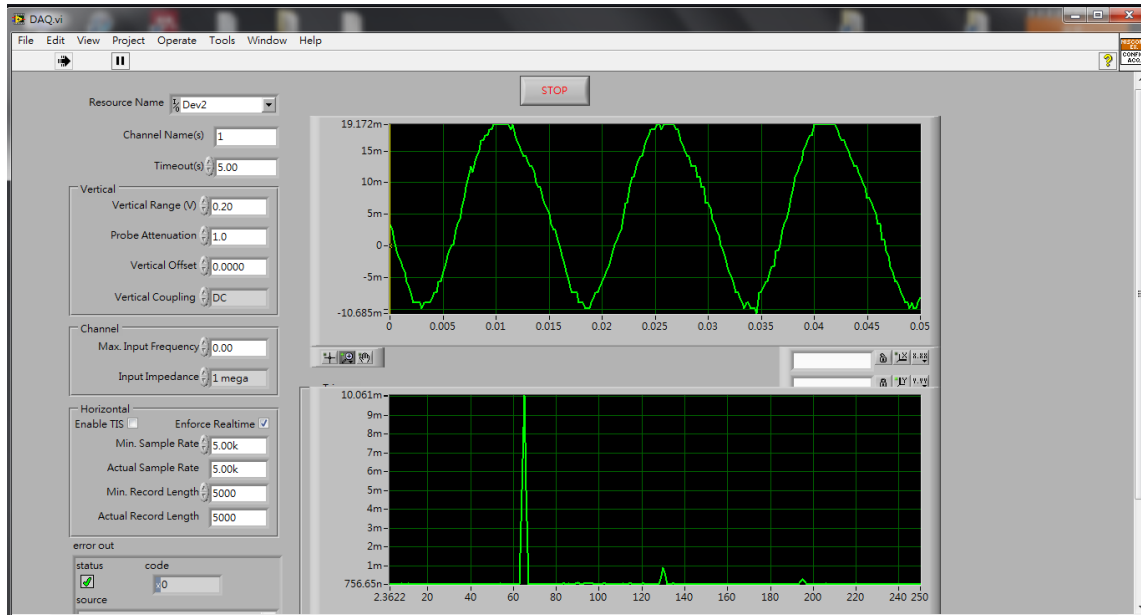


Fig. 3-7 Image of data reading with LabVIEW programming

In order to make sure that the frequency of the vibrated substrate read by the DAQ system (output signal) was as same as the frequency of the signals given by the PC (input signal), a mono-frequency calibration test was undertaken. Fig. 3-8 depicts the calibration curve which shows that input and output frequencies were linearly related.

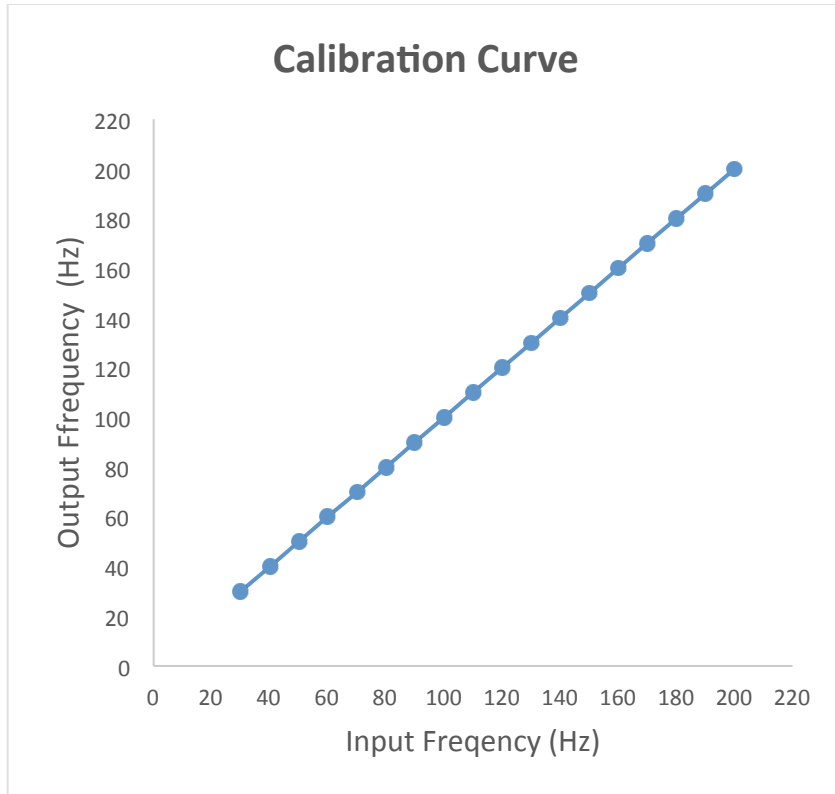


Fig. 3-8 Calibration curve of the output frequency and the input frequency

3.4 Image capture system

The dynamic images of droplets, including their vibration behaviors and the sliding processes, were captured using a high speed camera (Photron SA3) as shown in Fig. 3-9. The maximum speed of the camera was set at 60,000 frames per second, and the maximum view of vision was 1024×1024 pixel. The lens and the frame rate determine the resolution. High-resolution lens (zoom 6000 series lens Navitar) were used in this study.



Fig. 3-9 Image of the high speed camera used in this research

3.5 Hybrid surface

The hybrid surfaces were fabricated as part of a comprehensive condensation study (Yao et al. (2012) [33]). As seen in Fig. 3-10a and 3-10b, these structured surfaces includes hydrophilic silicon oxide (SiO_2) for the top sides of the micropillars, and a thin film of the hydrophobic material ($(\text{C}_2\text{F}_4)_n$) which covers the sides and troughs of the micropillar arrays. Three designs with edge-to-edge spacings of $25\ \mu\text{m}$, $37.5\ \mu\text{m}$, $50\ \mu\text{m}$, respectively were used in this study as shown in Fig. 3-11.

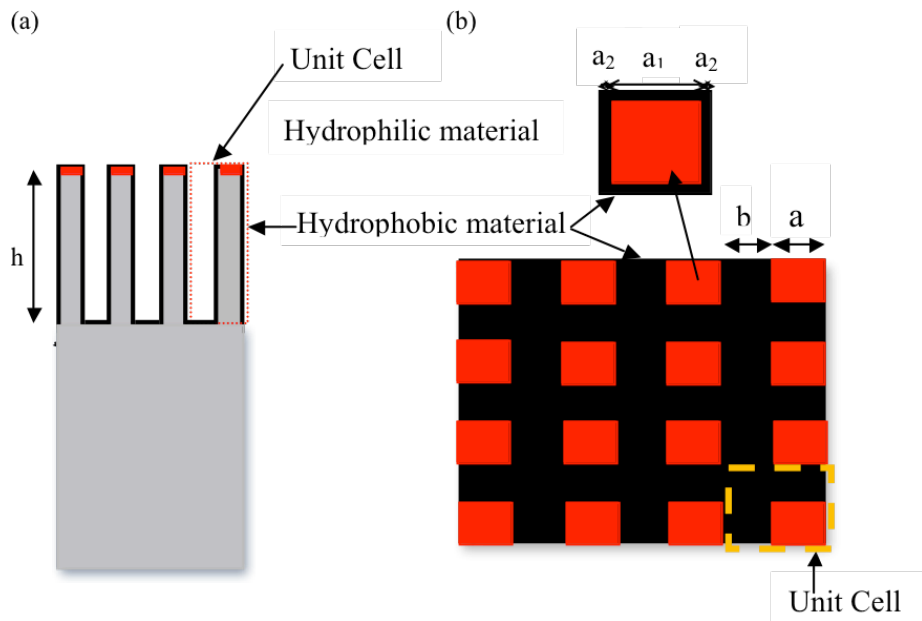


Fig. 3-10 Schematic drawings of (a) side view of the hybrid surface, (b) top view of a hybrid surface, where a_1 is the width of hydrophilic material, a_2 is the width of hydrophobic material [33]

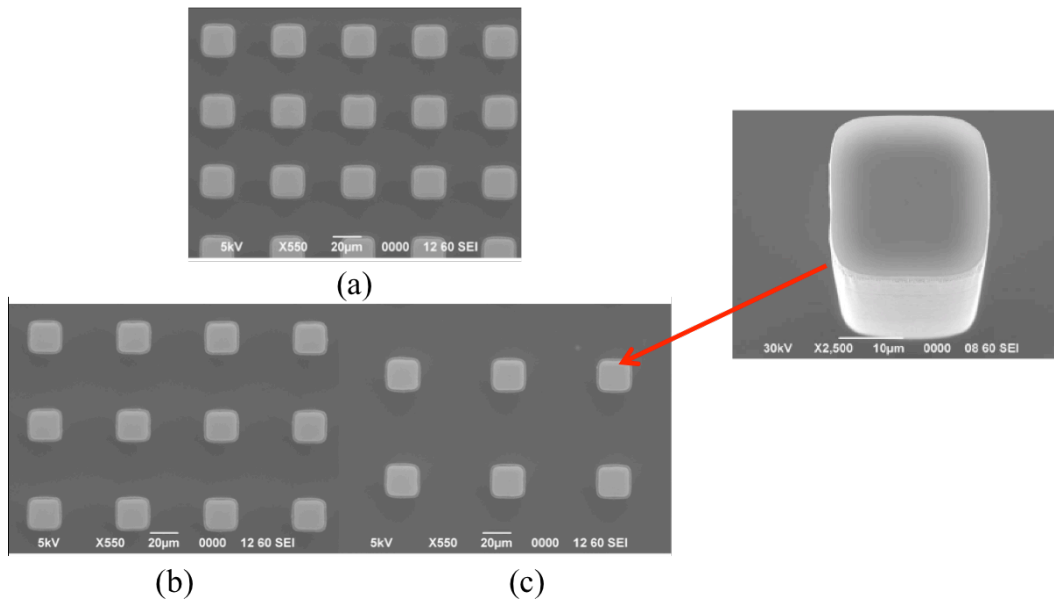


Fig. 3-11 SEM images of a hybrid surfaces with a micropillar array with spacing values of (a) $25\ \mu\text{m}$ (b) $37.5\ \mu\text{m}$, and (c) $50\ \mu\text{m}$ [33]

3.6 Procedures

The following subsections describe the experimental protocols used to measure contact angles, sliding angles, and natural resonance frequencies used in the study.

3.6.1 Contact angle measurement

Droplets were slowly placed on each horizontally-aligned surface using a pipette, and the images of each droplet was captured using the high speed camera. The contact angles of the droplets were measured using the software “Drop Shape Analysis” (a plugin for ImageJ). Fig. 3-12 provides an example of image used for measuring contact angle.

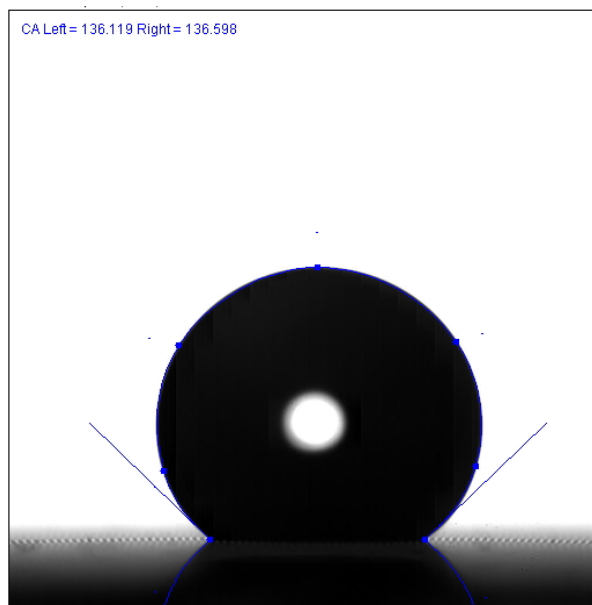


Fig. 3-12 Image of the contact angle measurement for 5- μm droplet on the hybrid surface with 25- μm spacing value

3.6.2 Sliding angle measurement

The test surfaces were horizontally fixed on the fine-tilting stage, and then the tilting stage system was inclined to a specific angle using the coarse-tilting stage. A droplet was slowly placed on the test surface. When the droplet became static, the system was slowly inclined with the fine-tilting stage until the droplet started to move. At that point, the inclined angle of the tilting-stage system was assumed to be the sliding angle of the droplet. The sliding process of the droplet was recorded using the high speed camera.

3.6.3 Resonance frequency of impinged droplets

To reduce sliding angle efficiently, the resonance frequency of each droplet were calculated taking into account droplet volume and static contact angle based on the Noblin et al. [31] and Boreyko et al. [13] equation as shown below. The basic idea relied on the use of resonance to facilitate droplet shedding. To that end, the theoretical droplet resonance model was used in conjunction with experimental data to identify the most suitable frequency modes that could improve shedding. The first two active resonance frequencies would be used to vibrate the tilting-stage system to investigate their effects on droplet sliding angles.

3.6.3.1 Theoretical values of droplet resonance frequency

The theoretical model proposed by Noblin et al. (2004) [31] and revised by Boreyko et al. (2009) [13] was used for predicting the resonance frequencies of droplets.

This model (Type-I of the Noblin et al. model) can be used to identify droplet oscillation placed on the structured surfaces at low-amplitude vibration as shown in Fig. 3.13. The theoretical values of droplet resonance frequencies were obtained using the following equations.

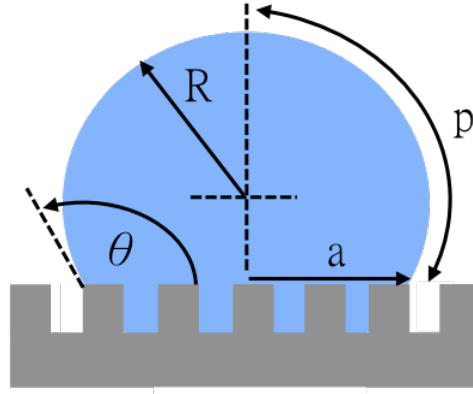


Fig. 3-13 Schematic drawing of a droplet with parameters used in the theoretical model [13]

$$\omega_j^2 = \left(g q_j + \frac{\gamma}{\rho} q_j^3 \right) \tanh \left(q_j \frac{V}{\pi a^2} \right) \quad (3-1)$$

$$q_j = \frac{\pi(j-0.5)}{p} \quad (3-2)$$

$$p = R\theta \quad (3-3)$$

$$R = \left(\frac{3V}{\pi(1-\cos\theta)^2(2+\cos\theta)} \right) \quad (3-4)$$

Where ω_j is resonance frequency corresponding to resonance mode number j , g is the gravitational acceleration, γ is the surface tension, ρ is the density of the droplet, V is the

drop volume, and a is the drop contact radius. The wave factor q_j for one dimensional capillary-gravity wave was calculated using Equation (3-2), where p the half arc length of a droplet was obtained from Equation (3-3) and (3-4). The apparent contact angle (θ) was measured as mentioned in the section 3.6.1. The theoretical values from Equation (3-1) to (3-4) were calculated using MATLAB for different droplet volumes (V) on different surfaces (θ) with different resonance modes (j).

3.6.3.2 Experimental values of droplet resonance frequency

The resonance frequencies of droplets were experimentally searched as well. Droplets were placed on the test surfaces fixed on top of the acoustic vibration system as shown in Fig 3.1. The input frequency of the acoustic vibration system was varied from 30 Hz to 200 Hz using a similar amplitude. Once the droplet experienced resonance vibration, the frequency was read by the DAQ system. This search process was repeated for different droplet volumes (5 μ L, 10 μ L, 15 μ L) on different surfaces (silicon wafer, hybrid surfaces with 25 μ m, 37.5 μ m, 50 μ m spacing) The resonance frequencies with the lowest and the second low values corresponded to the first and the second resonance modes, respectively were identified for all the combinations of droplets and surfaces.

3.6.3 Sliding angle measurement with resonance-based vibration

Once a droplet was placed on the test surface fixed on the tilting-stage system, the system frequency was set at the experimental droplet resonance frequency to vibrate each droplet vigorously. Then the tilting-stage system was slowly inclined until the

droplet began to move. Images of the droplet rolling off the surfaces were captured using the high speed camera. The inclined angle of the tilting-stage system was recorded as the sliding angle of each droplet under the applied vibrated conditions.

4. RESULTS AND DISCUSSION

In this section, droplet characteristics on hybrid surfaces are presented based on experimental observations. First, resonance frequencies of droplets were identified through calculations and experimentation. Resonance motions were observed and correlated to the primary and secondary resonance modes. Then, sliding angles under various vibrated conditions were measured when using mono-resonance frequency, multi-resonance frequencies, and amplitudes. The relationship between different vibrated conditions and sliding angles was further investigated to understand the effects of vibration on overcoming droplet hysteresis during droplet roll off events.

4.1 Wetting characteristics of droplets on hybrid surfaces

Water droplets exhibit different wetting characteristics on hybrid surfaces with different structured spacings. The following sections showed the results of measured contact angles and sliding angles of droplets on different hybrid surfaces. A silicon wafer (hydrophilic surface) was used as baseline in the study.

4.1.1 Measured contact angles

The apparent contact angles of droplets were measured by imaging each droplet at rest. The Droplet Analysis software was used to estimate contact angle by taking into account water properties and the morphology of the droplet using images captured by the camera. Examples of contact angle measurements are provided in Fig. 4-1. Table 4-1

and Fig. 4-2 shows the values of apparent contact angle for different droplet volumes on different surfaces.

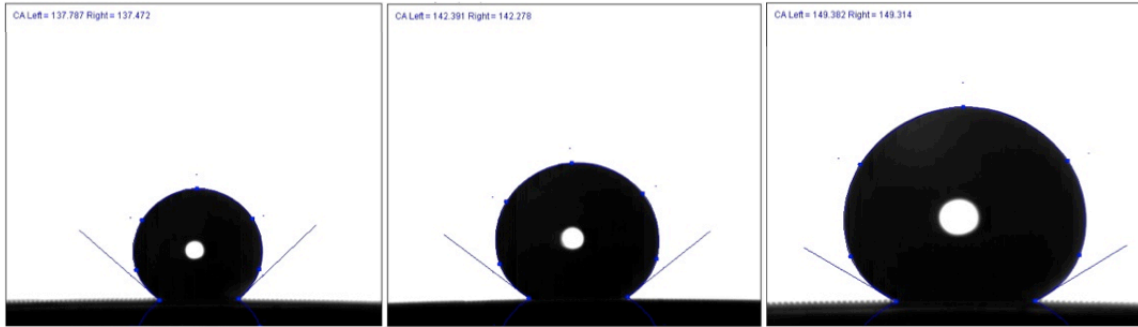


Fig. 4-1. Apparent contact angle measurement of three droplet volumes on a hybrid surface with 50 μm spacing

		Apparent Contact Angle ($^{\circ}$)		
		5	10	15
Droplet Volume (μL)				
Hybrid surface	50 μm	137.7	142.3	149.3
	37.5 μm	136.4	138.4	143.6
	25 μm	136.4	137.7	140.2
Silicon Wafer		34.2	35.6	37.4

Table 4-1 Apparent contact angles of droplets with different volumes on different surfaces

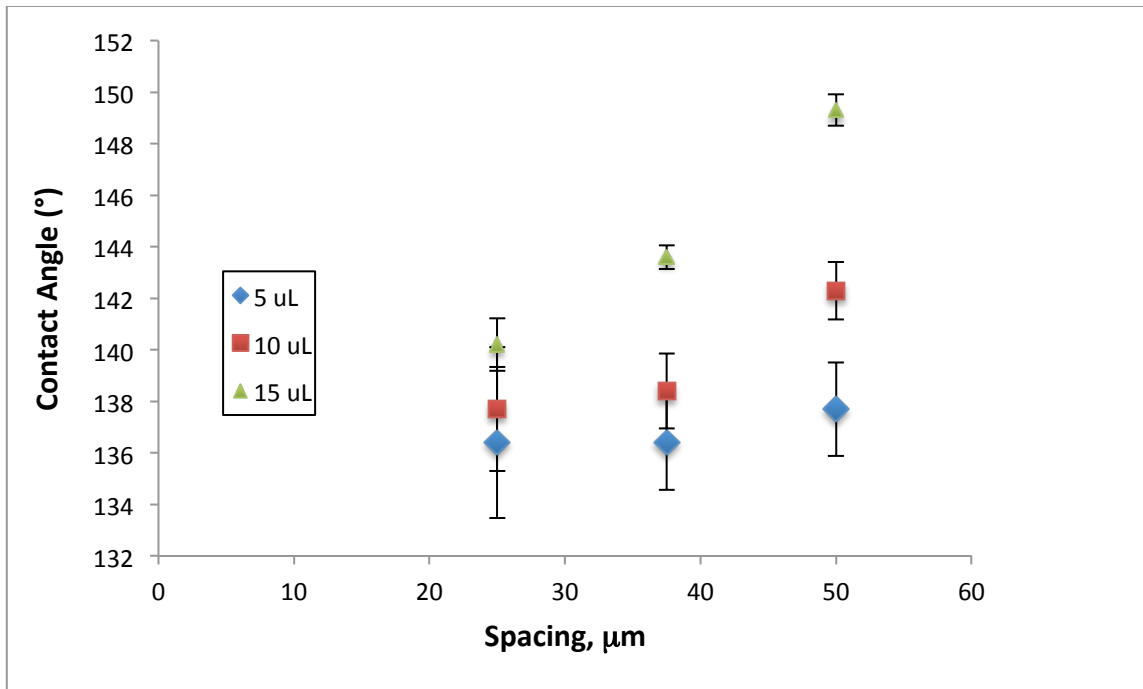


Fig. 4-2 Apparent contact angles of droplets with different volumes on different hybrid surfaces

As seen in Fig. 4-2, droplets with larger volume exhibit greater contact angle, specifically at higher micropillar spacing. He et al. (2004) also observed the same trend when droplet volume was increased, resulting in greater apparent contact angle until it reached a maximum static contact angle [34]. The increase in the apparent contact angle with volume can be attributed to the pinning of the droplet's contact line on the substrate. Once the advancing value of the contact angle is reached, the contact line moves and thereby causes no significant change in the apparent contact angle [34]. Droplets placed on hybrid surfaces with greater spacing exhibit a markedly hydrophobic behavior. Yao et al. (2012) also observed the same trend, which was consistent with the prediction from

the revised Cassie-Baxter equation (Yao et al. (2012)) as seen in Equation (4-1) to (4-3) [33].

$$\cos \theta_{ie} = x \cdot \cos \theta_1 + (1 - x) \cos \theta_2 \quad (4-1)$$

$$-1 + A(1 + \cos \theta_{ie}) = \cos \theta_a \quad (4-1)$$

$$A = \frac{a^2}{(a+b)^2} \quad (4-3)$$

Where intrinsic contact angle (θ_{ie}) of the top surface is calculated using Equation (4-1), where x represents relative area of the hydrophilic material with respect to the total top surface area, θ_1 is the contact angle of the liquid droplet on a flat hydrophilic surface, θ_2 is the contact angle of a liquid droplet on a flat hydrophobic surface. The equilibrium contact angles on the hybrid surface (θ_a) are predicted using Equation (4-2), and the area fraction A in Equation (4-3) is determined by knowing a and b which represent hydrophilic and hydrophobic lengths, respectively. From Equations (4-1) to (4-3), it is known that lower area fraction (A), which is caused by the hydrophobic area (b), results in greater equilibrium contact angle. Thus, the greater spacing always leads to a more pronounced hydrophobic behavior due in part to the presence of having more air trapped (i.e. air pockets) between each droplet and micropillars below.

4.1.2 Measured sliding angles

Droplet sliding angles on the static surfaces were measured as described in Section 3.6.2. Table 4-2 provides sliding angle values for different droplet volumes on different surfaces.

		Sliding Angle (°)		
		5	10	15
Droplet Volume (μL)				
Hybrid surface	50 μm	35.2	23.5	17.5
	37.5 μm	41.8	27.1	20.5
	25 μm	65.2	38.5	31.5
Silicon Wafer		DS	65.2	38.1

Table 4-2 Original sliding angles of droplets with different volumes on different surfaces. “DS” represents that a droplet does not move even at 90 °.

The data in Table 4-2 are also shown in Fig. 4-3, from which it can be observed that sliding angle decreases with increasing spacing of hybrid surfaces and droplet volume. Previous studies have shown that sliding angles increase as the weights of droplets decrease on both flat and rough surfaces once the dimension of the surface roughness is small enough with respect to the size of the droplet [19, 25, 35]. Miwa et al. also observed the similar trend when sliding angles decreased with decreasing surface roughness because of the high trapped-air ratio and small roughness values, which lead to better droplet shedding [19]. In this study, larger spacings of hybrid surface are

considered as small surface roughness, where lower sliding angles should be expected because of the high trapped-air ratio.

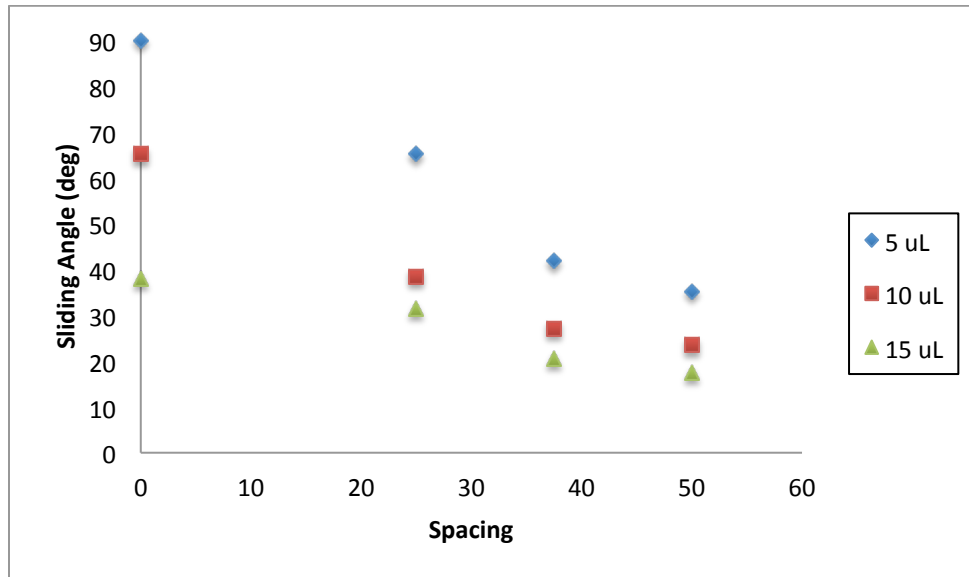


Fig. 4-3 Original sliding angles of droplets with different droplet volumes on different surfaces. Note: zero spacing represents the baseline (i.e. silicon wafer)

4.2 Resonance frequency of droplets

This section presents the results of resonance frequencies obtained from the Noblin’s model [31] and experiments, discusses the difference between the calculated and experimental values, and investigates the reason why the first resonance mode should be adjusted for 10 μL and 15 μL droplets to ensure adequate resonance behavior.

4.2.1 Calculated resonance frequency values and expected vibration behavior

The theoretical frequency values for adequate droplet resonance were calculated from the model mentioned in the section 3.6.3.1. The gravitational acceleration g was set to 9.81 m/s^2 , while surface tension (γ) and density of water (ρ) were set to 72.8 mN/s , and 998 kg/m^3 , respectively. The calculated results acquired from MATLAB are shown in Table 4-3.

		1 st Natural Frequency (Hz) j = 1.5			2 nd Natural Frequency (Hz) j = 2.0		
		5	10	15	5	10	15
Surface	Volume (μL)						
Hybrid surface	50 μm	60	39	33	108	68	57
	37.5 μm	61	43	34	109	76	60
	25 μm	60	43	35	108	77	62
Silicon Wafer		47	35	30	100	74	63

Table 4-3 Calculated frequency values for droplet resonance for different droplet volumes on different surfaces

The resonance modes (j) were set as 1.5 and 2, corresponding to the first and the second resonance frequencies, respectively. When droplets were vibrated at the first resonance frequency with j equal to 1.5, droplets were expected to exhibit lateral resonant motion with a pinned three-phase contact line as shown in Fig. 4-4b [13]. Lateral resonant motion of droplets has the most important effect on droplet mobility, because vibration induces an increase in advancing angle and a decrease in receding angle. Furthermore, the contact angle varies along the contact line resulting in an unbalanced condition which induces droplet motion under the effects of gravity as discussed in greater detail below. Moreover, when the droplet vibration is strong enough, it can overcome the droplet's contact angle hysteresis threshold which leads to droplet shedding [32] as presented below. When droplets vibrate at the second resonance frequency, they continuously stretch vertically and horizontally as shown in Fig. 4-4c [15, 16, 31]. In Section 4.3 the effects of frequency modes on sliding angle is discussed in greater detail.

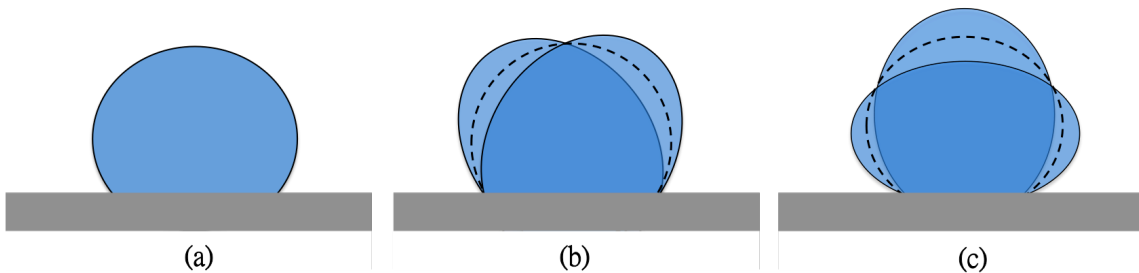


Fig. 4-4 Schematic drawing of expected droplet motions (a) without vibration (at static equilibrium), (b) at the first resonance frequency ($j = 1.5$), (c) at the second resonance frequency ($j = 2.0$). The dash line in (b) and (c) represents the droplet contour at static equilibrium.

4.2.2 Experimental resonance frequency values and droplet resonance behavior

The experimental frequency values for droplet resonance were obtained following the procedure described in Section 3.6.3.2 and are shown in Table 4-4.

		1 st Natural Frequency (Hz)			2 nd Natural Frequency (Hz)		
		5	10	15	5	10	15
Surface	Volume (μL)						
Hybrid surface	50 μm	61	54	46	109	68	58
	37.5 μm	62	54	45	109	71	61
	25 μm	62	54	49	108	71	62
Silicon Wafer		45	31	below 30	100	75	67

Table 4-4 Experimental frequency values for droplet resonance for different droplet volumes on different surfaces

As it can be seen in Tables 4-3 and 4-4, the experimental values agree well with the calculated ones when vibrating a 5 μL droplet. However, when droplet volume is increased between 10 and 15 μL , the difference between calculated and measured resonance frequencies become significant when the first natural frequencies are imposed.

To understand the effect of droplet volume on the difference between calculated and measured resonance frequencies, droplet vibration motion were recorded using a high speed camera. Fig. 4-5 shows different droplets vibrating at two distinct resonance frequencies on a 25 μm -spacing hybrid surface. Similar droplets motions were observed on 37.5 μm -spacing and 50 μm -spacing hybrid surfaces.

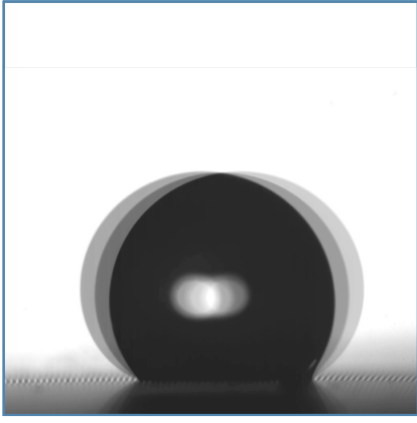
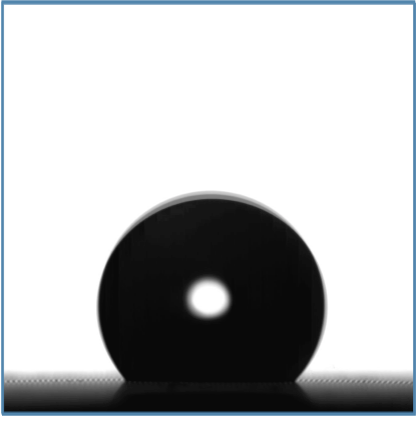
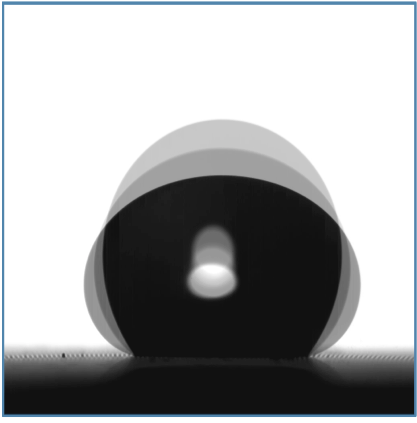
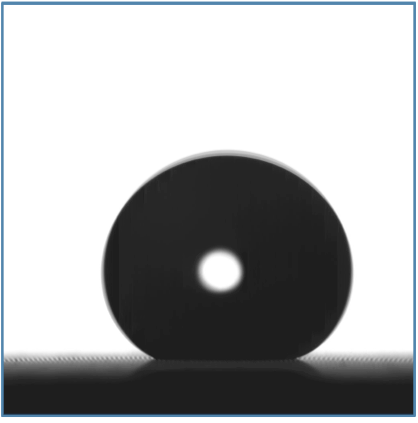
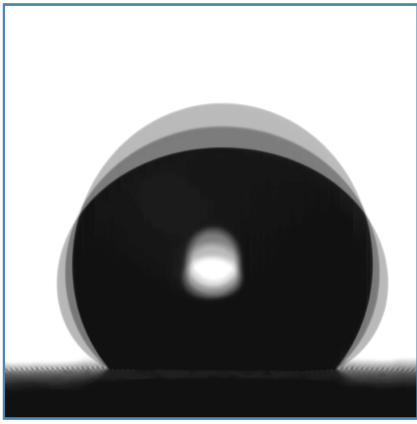
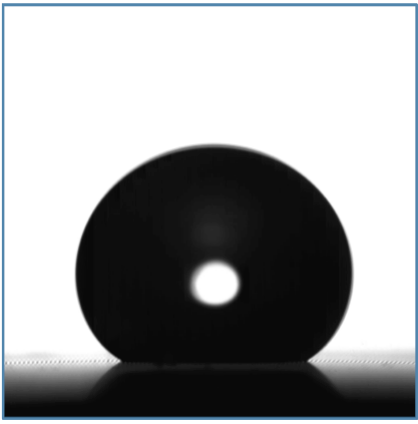
$V \backslash \omega$	1 ST Resonance Frequency	2 nd Resonance Frequency
5 μ L		
10 μ L		
15 μ L		

Fig. 4-5 Droplet resonance motions on the 25 μ m-spacing hybrid surface

As seen in Fig.4-5, it can be observed that the first resonance motions for 10 μL and 15 μL droplets are quite different from the 5 μL droplet. The 5 μL droplet exhibits significant lateral vibration which matches the prediction of droplet motions as shown in Fig. 4-4(b); while the 10 μL and 15 μL droplets displayed vertical resonance motions which are more common when the second resonance frequencies are imposed. It can be concluded that the first resonance frequencies for 10 μL and 15 μL droplets obtained from experiments correspond to a resonance mode (j) other than 1.5. On the other hand, when vibrating the droplets at the second resonance frequency, all the droplets continuously vibrate vertically and horizontally as predicted by the model, as shown in Fig. 4-4(c).

4.2.3 Natural Resonance Frequency Mode Adjustments for Optimal Droplet Vibration

In order to match experimental results of the first resonance frequencies, the resonance mode (j) was adjusted for the 10 μL and 15 μL droplets. It was found that the calculated values and the experimental results were similar once the resonance mode (j) was set equal to 1.7. Table 4-5 shows the calculated values with different resonance modes ($j=1.5, 1.7$) and the experimental frequency values for the 10 μL and 15 μL droplets. It is obvious that the calculated values when j equal is set equal to 1.7 agree better with the experimental results. This suggests that at greater droplet volumes, Equations 3-1 through 3-4 cannot account for the pinning effect that takes place between the droplets and the hybrid surfaces [33]. Furthermore, Yao et al. reported that the

pinning effect affects the motion of the contact line during droplet evaporation, which could explain why the calculated resonance frequency is not sufficient to induce droplet vibration under resonance conditions [33].

		10 μL Droplet			15 μL Droplet		
		Calculated Frequency (Hz)		Experimental Frequency (Hz)	Calculated Frequency (Hz)		Experimental Frequency (Hz)
		j = 1.5	j = 1.7		j = 1.5	j = 1.7	
Hybrid Surface	50 μm	39	54	54	33	42	46
	37.5 μm	43	56	54	34	44	45
	25 μm	43	56	54	35	45	49

Table 4-5 Calculated and experimental first resonance frequencies for 10 μL and 15 μL droplets

In order to differentiate droplet motion induced by resonance modes 1.5, 1.7 and 2.0, wave nodes along the droplet profile were taken into account. Previous studies observed three and four nodes along the droplet profile when droplets vibrated at resonance mode of 1.5 and 2.0, respectively. Fig. 4-6 shows the expected droplet motions with wave nodes for the resonance modes of 1.5 and 2.0 [13, 16, 31].

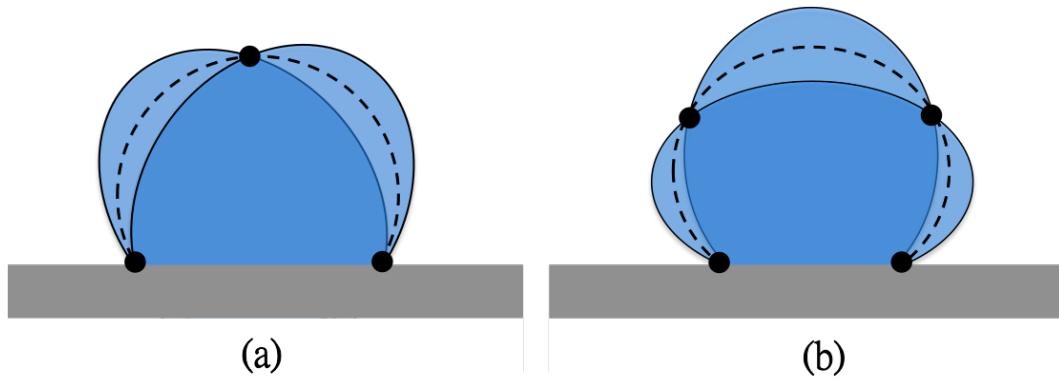


Fig. 4-6 Schematic drawing of expected droplet motions (a) at the first resonance frequency ($j = 1.5$, 3 nodes), (b) at the second resonance frequency ($j = 2.0$, 4 nodes). The dash line in (a) and (b) represents the droplet contour at static equilibrium, and the black spots emphasizes the nodes.

1st Resonance Frequency		
V	Experimental Image	Schematic Drawing
5 μ L		$j = 1.5$
10 μ L		$j = 1.0$
15 μ L		$j = 1.0$

Fig. 4-7 Experimental image and schematic drawing of the first resonance frequency for each droplet volume on a 25 μ m-spacing hybrid surface

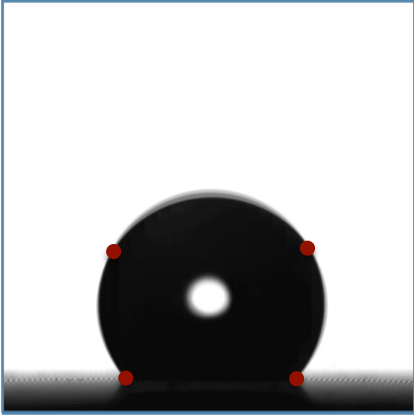
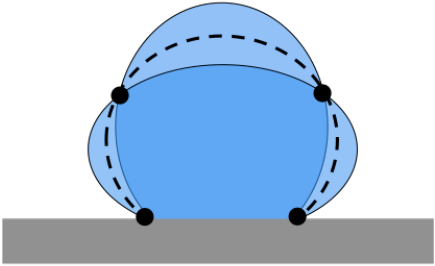
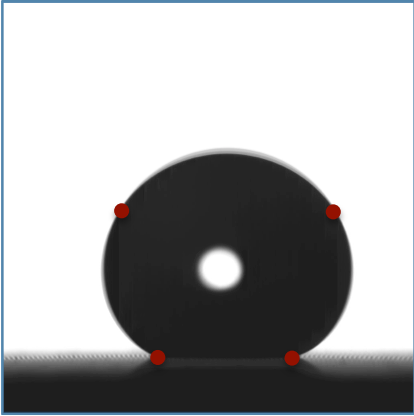
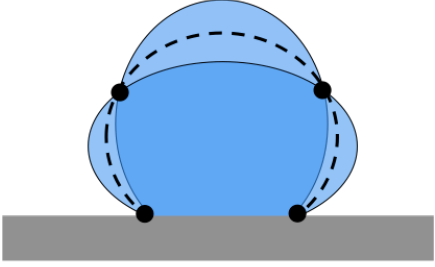
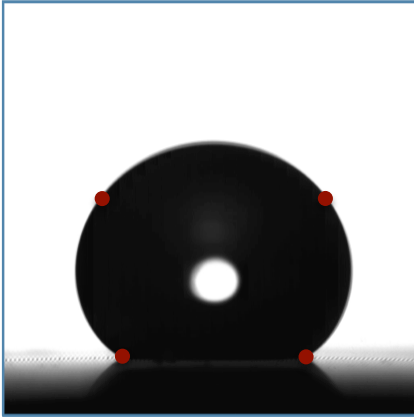
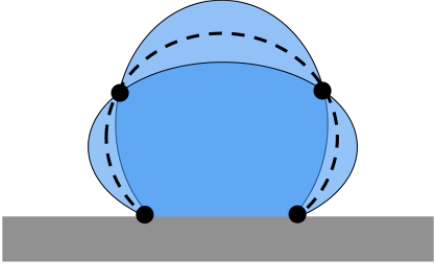
2 nd Resonance Frequency		
v	Experimental Image	Schematic Drawing
5 μ L		$j = 2.0$ 
10 μ L		$j = 2.0$ 
15 μ L		$j = 2.0$ 

Fig. 4-8 Experimental image and schematic drawing of the second resonance frequency for each droplet volume on a 25 μ m-spacing hybrid surface

Figures 4-7 and 4-8 show schematic drawings of specific droplet behaviors (Schematic Drawing) correspond to the experimental results of droplet motion (Experimental Image) taking account into wave nodes.

As seen in Fig. 4-7, when a 5 μL droplet vibrates at the first resonance frequency, it exhibits lateral resonance motion with three nodes corresponding to resonance mode of 1.5, while the 10 μL and 15 μL droplets exhibit vertical resonance motion with two nodes, which resembles the vibration behavior when the mode is set to 1.0 ($j = 1.0$) in Equations 3-1 through 3-4. The observed behavior suggest that droplets sitting on hybrid surface exhibit the same type of lateral and vertical resonance motion as the ones predicted by the equations [13, 31] even though the resonance frequencies do not match the values obtained using the equations as explained above. In Fig. 4-8, when vibrating at the second resonance frequency, 5 μL , 10 μL and 15 μL droplets vibrated vertically and horizontally continuously with four nodes corresponding to a resonance mode of 2.0. Therefore, it can be concluded that different resonance modes ($j = 1.5, 1.7, 2.0$) corresponds to distinct resonance motions by recognizing the number of nodes along droplet profile. Furthermore, when droplets sit on hybrid surfaces, their vibration behavior can be explained by previous studies [11, 16, 31] even under the influence of the pinning effect when considering a range of mode values.

From the first resonance frequency experiments, it is evident that the resonance modes for 10 μL and 15 μL droplets should be 1.7 instead of 1.5. Furthermore, the first observed resonance motion is mainly characterized by vertical resonance motion even though the 5 μL droplet vibrated laterally. The possible reason for this phenomenon

could be the effect of gravity on larger droplets. It is known that surface tension force is dominant at the micro scale; however, the influence of gravitational force could not be ignored for droplet with larger volumes. Evidence of the effect of gravity on large droplets can be seen in Fig. 4-9, where larger droplets are characterized by having a flattened configuration. On the hybrid surfaces, the shape of droplets with larger volume was more elliptical. The elliptical shape might impede the lateral resonance motion induced by the resonance mode of 1.5. Therefore, the resonance motion with resonance mode of 1.5 was subtle in the 10 μL and 15 μL droplets.

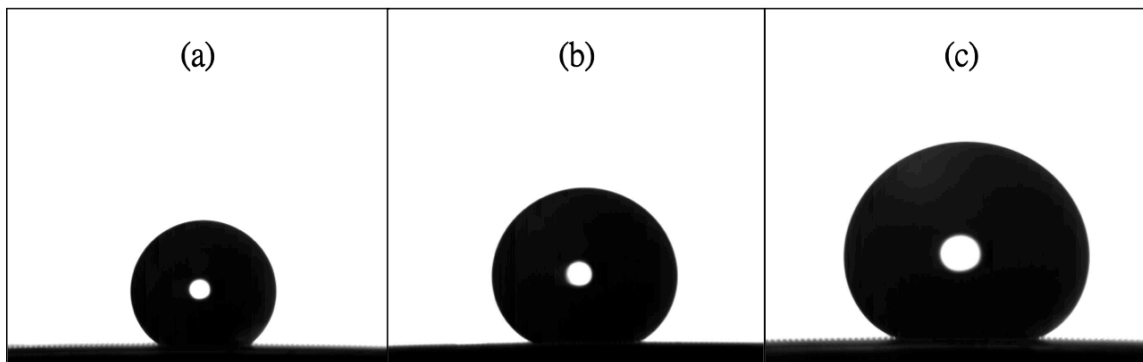


Fig. 4-9 The configuration of (a) 5 μL , (b) 10 μL , (c) 15 μL droplet on the hybrid surface with 50- μm spacing

4.3 Sliding angles under various vibrated conditions

Sliding behaviors of droplets under acoustic vibration were recorded as explain Section 3.6.4. The subsections below present experimental results of droplet sliding angles influenced by vibration. The resonance frequencies used for testing sliding angles were acquired experimentally as shown in Table 4-4.

4.3.1 Effects of mono-resonance frequency

The effect of resonance frequency was investigated by placing droplets on all the test surfaces. Droplets were continuously vibrated at either the first resonance frequency or the second resonance frequency when inclining the substrate. The corresponding sliding angles were recorded as shown in Table 4-6. The amplitudes of vibration were set to about 0.1 g, and the actual values (measured amp) read by the DAQ system were also recorded as shown in Table 4-6.

			w/o Vibration	1 st Resonance Frequency		2 nd Resonance Frequency	
			Sliding Angle	Sliding Angle	Measured Amp (g)	Sliding Angle	Measured Amp (g)
5 μL	Surface		Sliding Angle	Sliding Angle	Measured Amp (g)	Sliding Angle	Measured Amp (g)
	Hybrid surface (spacing)	50 μ m	35.2°	20.8°	0.096	25.5°	0.098
		37.5 μ m	41.8°	26.3°	0.093	34.4°	0.097
		25 μ m	65.2°	46.6°	0.107	52.9°	0.102
Silicon wafer (hydrophilic)		DS	DS	0.095	DS	0.099	
10 μL	Surface		Sliding Angle	Sliding Angle	Measured Amp (g)	Sliding Angle	Measured Amp (g)
	Hybrid surface (spacing)	50 μ m	23.5°	14.8°	0.094	15.8°	0.092
		37.5 μ m	27.1°	22.3°	0.099	26.3°	0.101
		25 μ m	38.5°	31.1°	0.093	37.3°	0.102
Silicon wafer (hydrophilic)		62.5°	61.5°	0.091	42.9°	0.098	
15 μL	Surface		Sliding Angle	Sliding Angle	Measured Amp (g)	Sliding Angle	Measured Amp (g)
	Hybrid surface (spacing)	50 μ m	17.5°	12.7°	0.080	14.3°	0.096
		37.5 μ m	20.5°	16.4°	0.079	18.8°	0.097
		25 μ m	31.5°	22.2°	0.083	25.6°	0.096
Silicon wafer (hydrophilic)		38.1°	N/A	N/A	37.2°	0.095	

Table 4-6 Droplet sliding angles measured at different mono- resonance frequencies.
Note: “DS” means that droplets stick on the surface, and “N/A” means that the experiment was not undertaken due to the limitation of instruments.

In order to understand the effect of mono-resonance frequency on the reduction in sliding angles when testing hybrid surfaces, the experimental data are presented in Table 4-6 and in Figures 4-10 to 4-12.

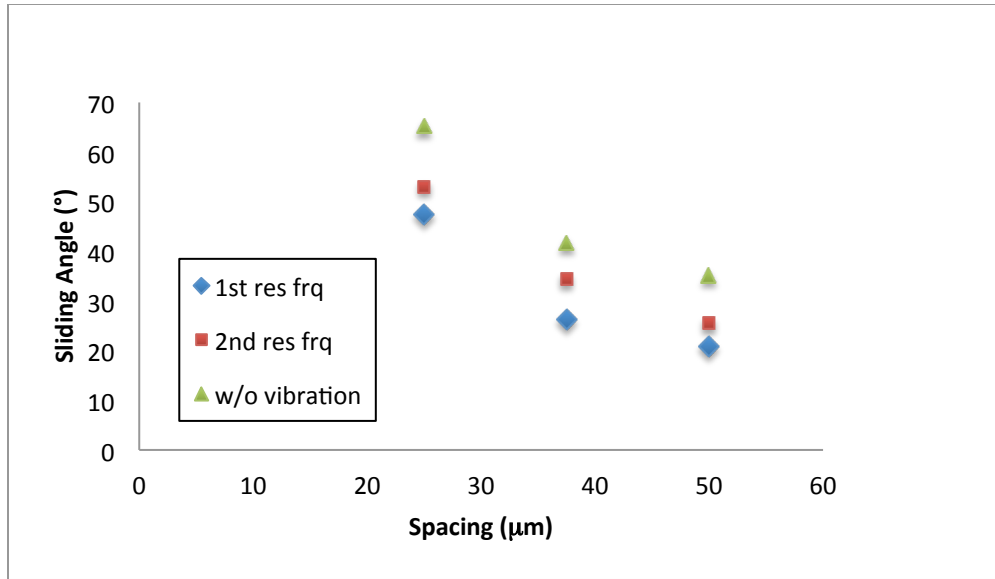


Fig. 4-10 Sliding angle of 5 μL droplet vibrating at different resonance frequencies

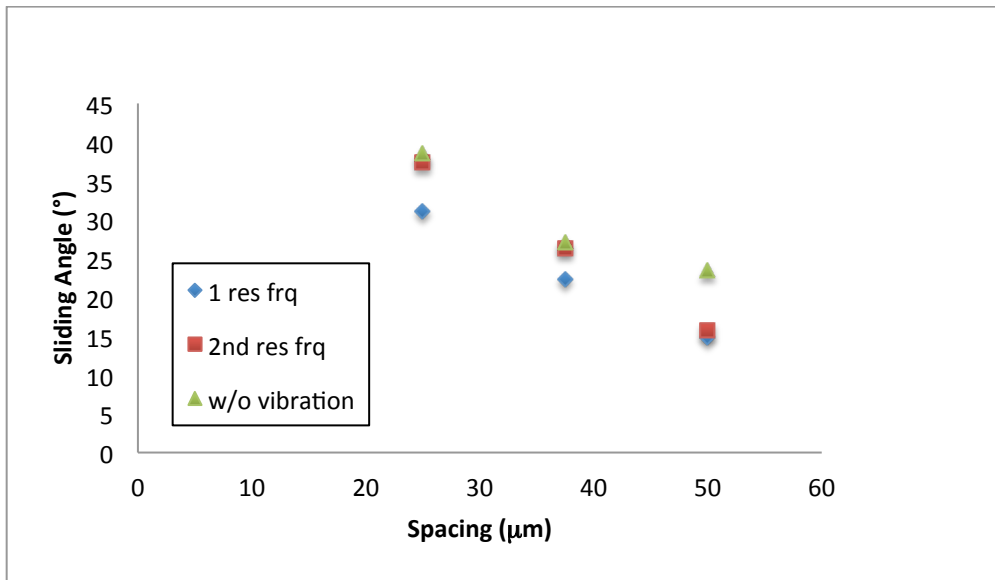


Fig. 4-11 Sliding angle of 10 μL droplet vibrating at different resonance frequencies

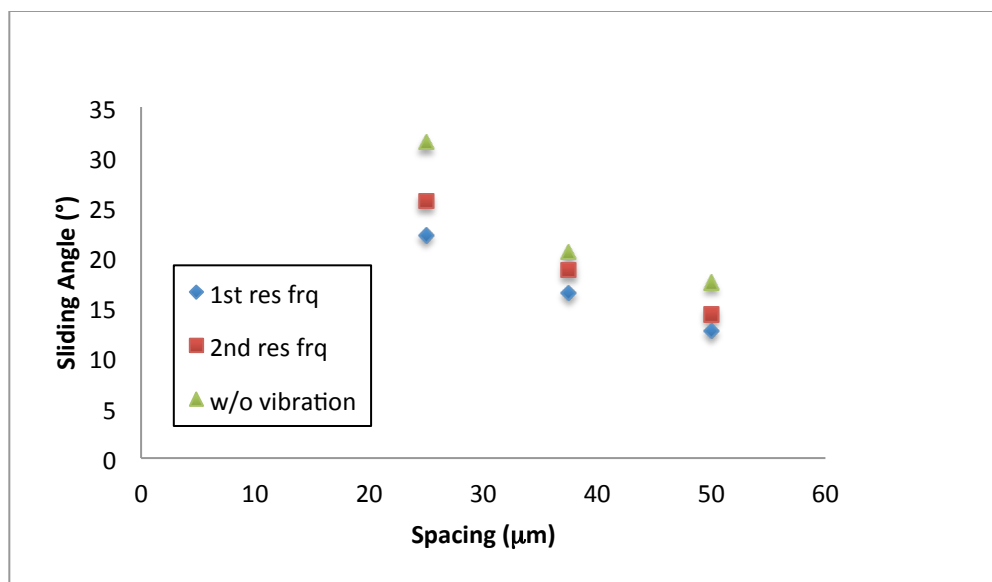


Fig. 4-12 Sliding angle of 15 μL droplet vibrating at different resonance frequencies

As seen in Fig 4-10 to Fig. 4-12, for different droplet volumes on hybrid surfaces with different spacings, the sliding angles (diamond and square spots) were entirely lower than original sliding angles (triangle spots) when vibrating at either the first or the second resonance frequencies. Furthermore, droplets vibrating at the first resonance frequency presented lower sliding angles (diamond spots) than when the droplets vibrated at the second resonance frequency (square spots). The difference between sliding angles resulting from the first and second resonance frequencies can be attributed to the droplet resonance motions shown in Figures 4-5, 4-7 and 4-8. The resonance motions for the first resonance frequencies were more active than those for the second resonance frequencies as seen in Fig. 4-5. One possible explanation for the significant decrease in sliding angle can be attributed to effect of vigorous lateral droplet motion, which helps overcome the droplet contact angle hysteresis effect easier. In the case of

hybrid surfaces, it has been reported that sliding angle is directly correlated to contact angle hysteresis [33]. In addition, previous studies [11, 13] show that the wetting transition is caused by the displacement of the triple line, which takes place once the amplitude threshold has been reached. Moreover, the threshold amplitude corresponding to the first resonance frequency is lower than the second resonance frequency [11]. Therefore, the first resonance frequency is more favorable for reducing sliding angles due to the lower threshold amplitude required for the dewetting transition.

From Fig. 4-10 to 4-12, it is evident that micropillar spacing has an effect of sliding angle which is consistent with the results obtained by Yao et al. [33]. From Table 4-6, it can be seen that droplet volume affects sliding angle considerably. Furthermore, both resonance frequencies helped reduce the sliding angle when the droplet volume was 15 μL .

4.3.2 Effects of 1st resonance amplitude

In order to understand the influence of vibrated intensity on sliding angles, droplets were vibrated at the first resonance frequency and two different amplitudes (0.05g and 0.1g). Table 4-7 shows sliding angles of droplets under different resonance amplitudes.

		w/o vibration	Lower Amp. (0.05g)		Higher Amp. (0.1g)		
	Surface	Sliding Angle	Sliding Angle	Measured Amp. (g)	Sliding Angle	Measured Amp. (g)	
5 μL	Hybrid surface (spacing)	50 μ m	35.2°	21.9°	0.052	20.8°	0.096
		37.5 μ m	41.8°	29.9°	0.051	26.3°	0.093
		25 μ m	65.2°	51.0°	0.056	46.6°	0.107
		Surface	Sliding Angle	Sliding Angle	Measured Amp. (g)	Sliding Angle	Measured Amp. (g)
10 μL	Hybrid surface (spacing)	50 μ m	23.5°	16.5°	0.052	14.8°	0.094
		37.5 μ m	27.1°	24.8°	0.051	22.3°	0.099
		25 μ m	38.5°	33.4°	0.046	31.1°	0.093
		Surface	Sliding Angle	Sliding Angle	Measured Amp. (g)	Sliding Angle	Measured Amp. (g)
15 μL	Hybrid surface (spacing)	50 μ m	17.5°	13.8°	0.039	12.7°	0.080
		37.5 μ m	20.5°	17.5°	0.036	16.4°	0.079
		25 μ m	31.5°	26.0°	0.040	22.2°	0.083
		Surface	Sliding Angle	Sliding Angle	Measured Amp. (g)	Sliding Angle	Measured Amp. (g)

Table 4-7 Droplet sliding angles measured at the first resonance frequency with different amplitudes

Fig. 4-13 to Fig. 4-15 show that droplets with different volumes vibrating at higher amplitude exhibited lower sliding angles. It is known that once the threshold amplitude corresponding to the resonance frequency is reached, the triple line of a droplet is able to move continuously [11, 13]. Furthermore, when droplets vibrate at larger amplitudes after reaching the amplitude threshold, droplet hysteresis should be easier to overcome leading to the downward displacement of the droplet triple line on the inclined surface. It can be concluded that larger amplitudes are favorable to reduce sliding angles. Moreover, larger amplitudes involve greater acoustic energy that could explain why droplets exhibit lower sliding angles on hybrid surfaces.

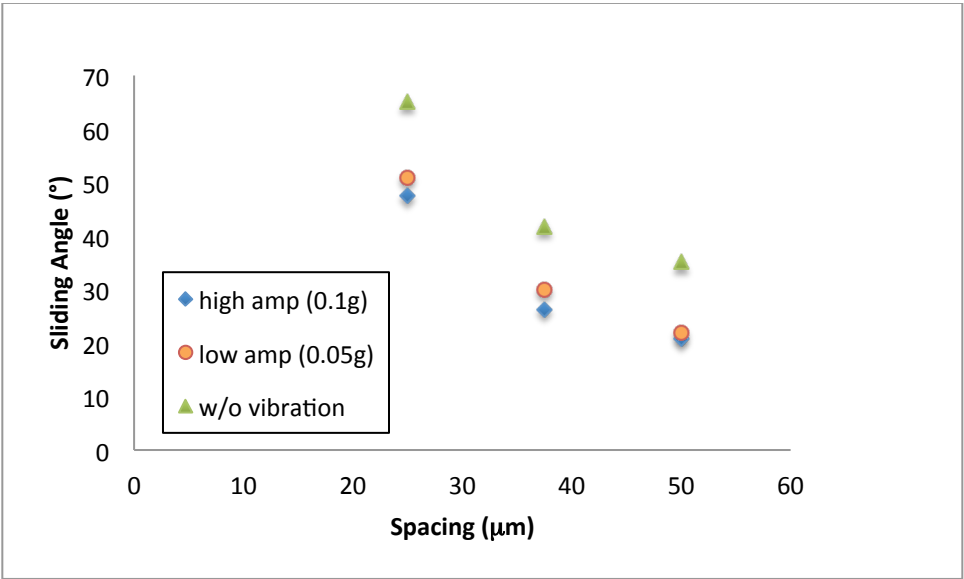


Fig. 4-13 Sliding angle of 5 μL droplet vibrating at the first resonance frequencies with different amplitudes

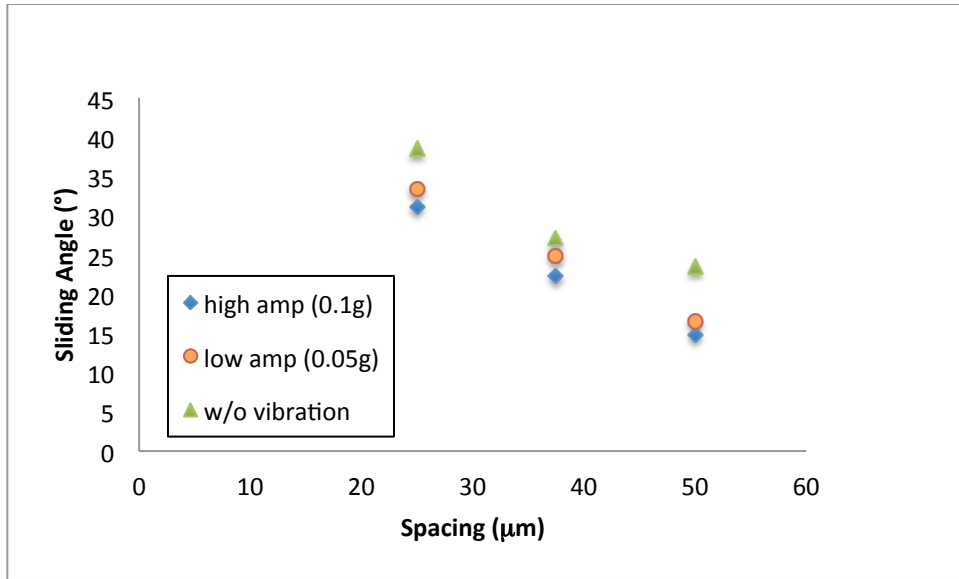


Fig. 4-14 Sliding angle of 10 μL droplet vibrating at the first resonance frequencies with different amplitudes

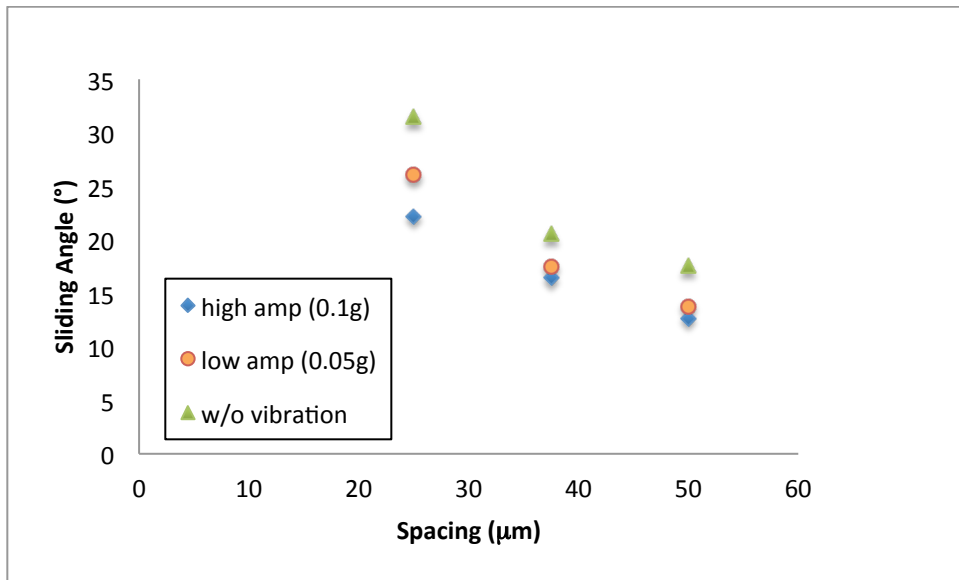


Fig. 4-15 Sliding angle of 15 μL droplet vibrating at the first resonance frequencies with different amplitudes

4.3.3 Effects of multi-resonance frequencies

Multiple-resonance frequencies were used to determine their effects on sliding angle. From the experiments, it is evident that droplet sliding angles were effectively reduced when using single resonance frequency as mentioned in Section 4.3.1. However, sliding angles of small droplets (5 μ L droplets), were still not low enough when vibrated at mono-resonance frequency. Furthermore, the difference between sliding angles when using first and second resonance frequencies is more significant at low droplet volumes as shown in Table 4-6. Moreover, little is known about the effect of multiple-resonance frequencies on sliding angle. Therefore, multiple-resonance frequencies were applied consecutively to the droplets using the first and second resonance frequencies (one second per frequency) as shown in Table 4-4. Table 4-8 shows the sliding angles of 5 μ L droplets on different hybrid surfaces vibrating at two frequencies (first and second resonance frequencies).

Hybrid Surface	w/o vibration	1 st Resonance Frequency		2 nd Resonance Frequency		Multi-Frequency		
	Sliding Angle	Sliding Angle	Measured Amp. (g)	Sliding Angle	Measured Amp. (g)	Sliding Angle	Measured Amp, 1st (g)	Measured Amp, 2nd (g)
50 μ m	35.2°	20.8°	0.096	25.5°	0.098	22.5°	0.041	0.042
37.5 μ m	41.8°	26.3°	0.093	34.4°	0.097	31.9°	0.017	0.039
25 μ m	65.2°	46.6°	0.107	52.9°	0.102	45.1°	0.037	0.041

Table 4-8 Sliding angles of 5 μ L droplets measured at mono- or multi- resonance frequencies

Figure 4-16 shows the effects of first resonance frequency (diamond spots), second resonance frequency (square spots) and multi-frequency (round spots) on sliding angle for multiple micropillar spacing on the surfaces. In the cases of hybrid surfaces with 50 μm and 37.5 μm spacing, sliding angles of the 5 μL droplets were reduced when using multi-frequencies when compared to the second resonance frequency cases. However, the first resonance frequency cases resulted in lower sliding angles than when multi-frequencies were used. On the other hand, in the case of hybrid surface with 25 μm spacing, multi-frequency vibration resulted in a lower sliding angle than either the first or the second mono-resonance frequency cases.

From Figure 4-16, it can be seen that multi-resonance frequencies are more effective than using first or second resonance frequency when the micropillar spacing is small. It is known that first and second resonance frequencies result in different droplet motions from Figures 4-7 and 4-8. When multi-resonance frequencies are applied consecutively, the lateral motion observed by the 5 μL droplet in Figure 4-7 would be limited by imposing the second resonance frequency every other second. This suggests that lateral motion should be constrained somewhat when droplet contact angle hysteresis is high to be able to reduce sliding angle.

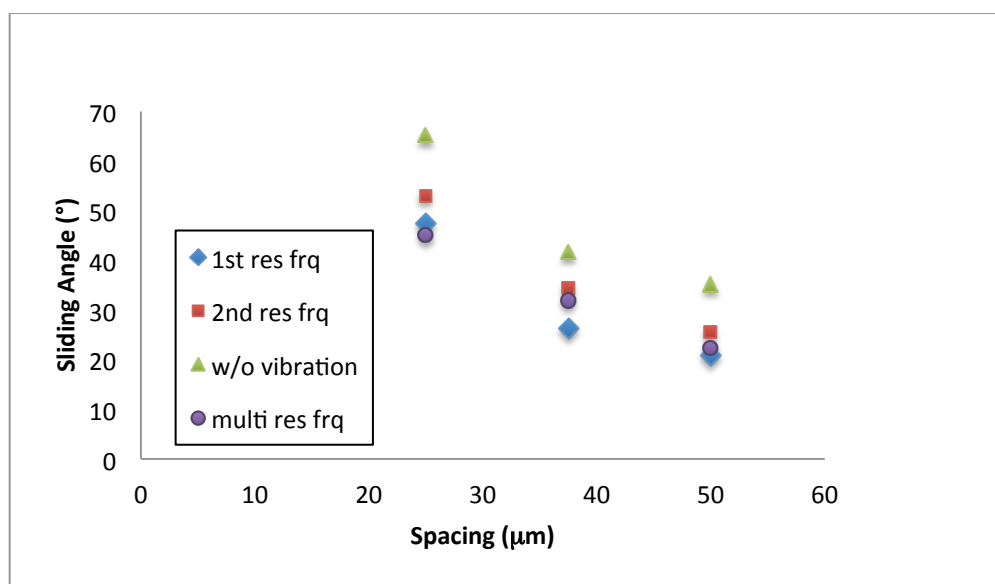


Fig. 4-16 Sliding angle of 5 μL droplet vibrating at mono- or multi- resonance frequencies

The effects of droplet volume and multi-frequencies on sliding angles are shown in Table 4-9.

		w/o vibration	1 st Resonance Frequency		2 nd Resonance Frequency		Multi-Frequency		
Hybrid Surface	Droplet Volume	Sliding Angle	Sliding Angle	Measured Amp. (g)	Sliding Angle	Measured Amp. (g)	Sliding Angle	Measured Amp, 1 st (g)	Measured Amp, 2 nd (g)
25 μm	5 μL	65.2°	46.6°	0.107	52.9°	0.102	45.1°	0.037	0.041
	10 μL	38.5°	31.1°	0.093	37.3°	0.102	30.3°	0.086	0.081
	15 μL	31.5°	22.2°	0.083	25.6°	0.096	26.7°	0.072	0.075

Table 4-9 Sliding angles of droplets with three different volumes measured at mono- or multi-resonance frequencies on a hybrid surface with 25 μm spacing

Table 4-9 shows that vibrating 5 μL and 10 μL droplets using multi-frequencies result in lower sliding angles. Contrarily, 15 μL droplet vibrated by multi-frequencies shows higher sliding angles than in the other two cases. This shows the limitations of using multi-frequencies to promote lower sliding angles. Furthermore, experimental observations confirmed that using multi-frequencies were ineffective in actuating larger droplets possibly because of droplet weight at low acoustic amplitudes. Moreover, it appears that using multiple frequencies consecutively inhibits the complete droplet motion seen when mono-frequencies are used, which in turn result in higher sliding angles in large droplets.

5. CONCLUSION

This research investigates the effects of hybrid surface morphology and acoustic vibration on droplet removal from surfaces used for condensation. The relationship between droplet sliding angles and droplet volumes on hybrid surfaces with different structured spacings was firstly investigated through experimentation. Then, the effects of natural resonance frequencies of droplets with different volumes on different surfaces were also studied and analyzed using a resonance model and a customized experimental setup. Acoustic-induced vibrations were then applied to the surfaces to understand the effects of single or multiple resonance frequencies on droplet sliding angles. Droplet vibration and sliding processes were experimentally characterized using a high speed imaging system and an acoustic sensing device.

From the experimental observation of droplet characteristics on hybrid surfaces, droplets with larger volume placed on hybrid surfaces with greater spacing exhibit greater apparent contact angles. The pinning of the droplet's contact line on the substrate leads to an increase in the apparent contact angle with volume, while higher air trapped ratio results in more hydrophobicity on hybrid surfaces with greater spacing. Moreover, droplet sliding angle decreases with increasing droplet volume and spacing of hybrid surfaces. Furthermore, experiments reveal that sliding angles decrease as hybrid surface's spacings increase because of the high trapped-air ratio and small roughness values, which lead to better droplet shedding.

From the results of droplet resonance frequency study obtained from the theoretical model and experimental observations, the resonance motions and calculated

resonance modes of the first resonance frequency were found to be different for different droplet volumes. Furthermore, a 5 μL droplet vibrating at the first resonance frequency exhibits lateral resonance motion with three wave nodes corresponding to the resonance mode of 1.5, while the 10 μL and 15 μL droplets exhibit vertical resonance motions with two wave nodes corresponding to the resonance mode of 1.7. The difference in behavior can be attributed to the effect of gravity on larger droplets which exhibit a flattened configuration, which impedes the lateral resonance motions induced by the resonance mode of 1.5. On the other hand, when vibrating the droplets at the second resonance frequency, all the droplets exhibit continuously vertical and horizontal vibration with four wave nodes corresponding to the resonance mode of 2.0.

The experimental droplet vibration results show that sliding angles decrease with first or the second resonance frequencies at different droplet volumes on hybrid surfaces with different spacings. Furthermore, droplets vibrating at the first resonance frequency always exhibited lower sliding angles than when the droplets vibrated at the second resonance frequency. This can be attributed to the first resonance frequency more active resonance motions and lower threshold amplitude required for the dewetting transition. Furthermore, observations reveal that the first resonance frequencies can be used to overcome the droplet contact angle hysteresis effect easier. In addition, larger amplitudes are favorable since they can reduce sliding angles because of the greater amount of acoustic energy available for overcoming contact angle hysteresis on the hybrid surfaces.

Multiple-resonance frequencies were also investigated to determine their effects on sliding angle. Multiple-resonance frequencies were applied consecutively to the

droplets using the first and second resonance frequencies. It was found that multi-resonance frequency cases are more effective than the second resonance frequency cases on reducing sliding angles. Moreover, when 5- μ L droplets were vibrated using multi-frequencies on a 25- μ m spacing surface, the reduction in sliding angle was better than in the other two mono-frequency cases. This suggests that lateral motion should be constrained somewhat when droplet contact angle hysteresis is high to be able to reduce sliding angles.

The study shows that resonance-based vibrations are effective in reducing sliding angles on a variety of hybrid surfaces. Future studies should consider the effects of acoustic vibration on droplet shedding during condensation.

REFERENCES

- [1] Fürstner, R. and W. Barthlott, *Wetting and Self-Cleaning Properties of Artificial Superhydrophobic Surfaces*. Langmuir, 2005. **21**: p. 956-961.
- [2] Bhushan, B., Y.C. Jung, and K. Koch, *Self-Cleaning Efficiency of Artificial Superhydrophobic Surfaces*. Langmuir, 2009. **25**(5): p. 3240–3248.
- [3] Cheng, K., et al. *Biomimetic Super-Hydrophobic Surfaces for Use in Enhanced Dropwise Condensation*. in *SPIE*. 2011.
- [4] Dietz, C., et al., *Visualization of Droplet Departure on a Superhydrophobic Surface and Implications to Heat Transfer Enhancement During Dropwise Condensation*. Appl. Phys. Lett., 2010. **97**(3): p. 033104.
- [5] Varanasi, K.K. and T. Deng, *Controlling Nucleation and Growth of Water Using Hybrid Hydrophobic-Hydrophilic Surfaces*, in *12th IEEE Intersociety Conference on Thermal and Thermomechanical Phenomena in Electronic Systems*. 2010.
- [6] Drelich, J., et al., *Contact Angles for Liquid Drops at a Model Heterogeneous Surface Consisting of Alternating and Parallel Hydrophobic/Hydrophilic Strips*. Langmuir, 1996. **12**(7): p. 1913-1922.
- [7] Morita, M., et al., *Macroscopic-Wetting Anisotropy on the Line-Patterned Surface of Fluoroalkylsilane Monolayers*. Langmuir, 2005. **21**(3): p. 911-918.
- [8] Varanasi, K.K., et al., *Spatial Control in the Heterogeneous Nucleation of Water*. Appl. Phys. Lett., 2009. **95**(9): p. 094101.

- [9] Saha, A.A. and S.K. Mitra, *Numerical Study of Capillary Flow in Microchannels With Alternate Hydrophilic-Hydrophobic Bottom Wall*. J. Fluids Eng., 2009. **131**(6): p. 061202.
- [10] Cassie, A.B.D. and S. Baxter, *Wettability of Porous Surfaces*. Trans. Faraday Soc., 1944. **40**: p. 546-551.
- [11] Bormashenko, E., et al., *Resonance Cassie-Wenzel Wetting Transition for Horizontally Vibrated Drops Deposited on a Rough Surface*. Langmuir, 2007. **23**: p. 12217-12221.
- [12] Brunet, P., J. Eggers, and R.D. Deegan, *Vibration-Induced Climbing of Drops*. Phys. Rev. Lett., 2007. **99**: p. 144501.
- [13] Boreyko, J. and C.-H. Chen, *Restoring Superhydrophobicity of Lotus Leaves with Vibration-Induced Dewetting*. Phys. Rev. Lett., 2009. **103**(17).
- [14] Bormashenko, E., et al., *Vibration-Induced Cassie-Wenzel Wetting Transition on Rough Surfaces*. Appl. Phys. Lett., 2007. **90**(20): p. 201917.
- [15] Jung, Y.C. and B. Bhushan, *Dynamic Effects Induced Transition of Droplets on Biomimetic Superhydrophobic Surfaces*. Langmuir, 2009. **25**(16): p. 9208-18.
- [16] Ramos, S.M.M., *Vertical Vibration of Liquid Drops on Nano-Structured Surfaces*. Nuclear Instruments and Methods in Physics Research Section B: Beam Interactions with Materials and Atoms, 2008. **266**(12-13): p. 3143-3147.
- [17] White, L.R., *On Deviations from Young's Equation* J. Chem. Soc., Faraday Trans. 1, 1977. **73**: p. 390-398.

- [18] Wenzel, R.N., *Resistance of Solid Surfaces to Wetting by Water*. Ind. Eng. Chem., 1936. **28**(8): p. 988-994.
- [19] Miwa, M., et al., *Effects of the Surface Roughness on Sliding Angles of Water Droplets on Superhydrophobic Surfaces*. Langmuir, 2000. **16**: p. 5754-5760.
- [20] Patankar, N.A., *On the Modeling of Hydrophobic Contact Angles on Rough Surfaces*. Langmuir, 2003. **19**: p. 1249-1253.
- [21] Patankar, N.A., *Transition between Superhydrophobic States on Rough Surfaces*. Langmuir, 2004. **20**: p. 7097-7102.
- [22] Albenge, O., et al., *Experimental Procedure to Measure the Blocking Energy of Liquid on Smooth Hydrophobic Surfaces*. Langmuir, 2002. **18**: p. 8929-8932.
- [23] Hyv aluoma, J., et al., *Droplets on Inclined Rough Surfaces*. Eur Phys J E Soft Matter, 2007. **23**(3): p. 289-93.
- [24]  ner, D. and T.J. McCarthy, *Ultrahydrophobic Surfaces. Effects of Topography Length Scales on Wettability*. Langmuir, 2000. **16**: p. 7777-7782.
- [25] Yoshimitsu, Z., et al., *Effects of Surface Structure on the Hydrophobicity and Sliding Behavior of Water Droplets*. Langmuir, 2002. **18**: p. 5818-5822.
- [26] ElSherbini, A.I. and A.M. Jacobi, *Critical Contact Angles for Liquid Drops on Inclined Surfaces*. Progress in Colloid and Polymer Science 2004: p. 57-62.
- [27] Ravi Annapragada, S., J.Y. Murthy, and S.V. Garimella, *Prediction of Droplet Dynamics on an Incline*. International Journal of Heat and Mass Transfer, 2012. **55**(5-6): p. 1466-1474.

- [28] Kelvin, L., *Oscillations of a Liquid Sphere*. Mathematical and Physical Papers, 1890. **3**: p. 384-386.
- [29] Rayleigh, L., *The Theory of Sound*. 1894, London: MacMillan.
- [30] Lamb, H., *Hydrodynamics*. 1932, Cambridge University Press: UK.
- [31] Noblin, X., A. Buguin, and F. Brochard-Wyart, *Vibrated Sessile Drops: Transition between Pinned and Mobile Contact Line Oscillations*. Eur Phys J E Soft Matter, 2004. **14**(4): p. 395-404.
- [32] Celestini, F. and R. Kofman, *Vibration of Submillimeter-Size Supported Droplets*. Physical Review E, 2006. **73**(4).
- [33] Yao, C.W., et al., *Droplet Contact Angle Behavior on a Hybrid Surface with Hydrophobic and Hydrophilic Properties*. Appl. Phys. Lett., 2012. **101**: p. 111605.
- [34] He, B., J. Lee, and N.A. Patankar, *Contact Angle Hysteresis on Rough Hydrophobic Surfaces*. Colloids and Surfaces A: Physicochemical and Engineering Aspects, 2004. **248**(1-3): p. 101-104.
- [35] Murase, H., et al., *Interactions Between Heterogeneous Surfaces of Polymers and Water*. Journal of Applied Polymer Science, 1994. **54**(13): p. 2051-2062.